

T-3113

A DIAGRAM TO PREDICT ALUMINUM PASSIVATED STAINLESS STEEL
WELD METAL MICROSTRUCTURE

Bernie Carpenter

ProQuest Number: 10782742

All rights reserved

INFORMATION TO ALL USERS

The quality of this reproduction is dependent upon the quality of the copy submitted.

In the unlikely event that the author did not send a complete manuscript and there are missing pages, these will be noted. Also, if material had to be removed, a note will indicate the deletion.



ProQuest 10782742

Published by ProQuest LLC (2018). Copyright of the Dissertation is held by the Author.

All rights reserved.

This work is protected against unauthorized copying under Title 17, United States Code
Microform Edition © ProQuest LLC.

ProQuest LLC.
789 East Eisenhower Parkway
P.O. Box 1346
Ann Arbor, MI 48106 – 1346

T-3118

A thesis submitted to the Faculty and the Board of Trustees of the Colorado School of Mines in partial fulfillment of the requirements for the degree of Master of Science (Metallurgical Engineering)

Golden, Colorado

Date 18 October 1985

Signed:



Bernie F. Carpenter

Approved:


David L. Olson
Thesis Advisor

Golden, Colorado

Date October 18, 1985


William D. Copeland
Head of Department
Metallurgical Engineering

ABSTRACT

The Fe-Mn-Ni-Al alloy system has been investigated as a potential replacement for traditional Fe-Cr-Ni stainless steel filler materials. In the Fe-Mn-Ni-Al alloys the microstructures are primarily austenite, due to the stabilizing effect of nickel and manganese, and derive their oxidation resistance from the aluminum. Systematic variations of nickel, manganese, and aluminum were made to a series of experimental bead-on-plate welds. The fusion zone microstructures were analyzed by optical microscopy, x-ray diffraction phase analysis, bulk chemical analysis, and microprobe scanning techniques. Based on these results the stable phases for a variety of alloy compositions have been determined, and are reported in terms of a "Schaeffler type" diagram. Alloys containing less than five weight percent aluminum were found to solidify as primary austenite and transform martensitically if insufficient alloy additions were present to suppress the martensite start temperature below room temperature. With manganese additions two different martensites were identified: the conventional BCT martensite, and an HCP epsilon martensite. Alloys containing greater than five weight percent aluminum have duplex microstructures of austenite and ferrite. The two martensitic

transformations were found to be independent parallel processes, each having its own composition dependent M_s temperature. In the duplex microstructures the weld metal ferrite appears similar to delta ferrite in Fe-Cr-Ni stainless steel weldments. The new Fe-Mn-Ni-Al alloys are weldable and are expected to be viable alternatives for traditional Fe-Cr-Ni filler materials.

TABLE OF CONTENTS

	<u>Page</u>
ABSTRACT	iii
LIST OF FIGURES	vi
LIST OF TABLES	viii
ACKNOWLEDGEMENTS	ix
I. INTRODUCTION	1
I.1 Strategic Significance	1
I.2 Oxidation/Sulfidization Behavior	8
I.3 Phase Diagrams	15
Fe-Mn-Al Ternary System	15
Fe-Ni-Al Ternary System	17
I.4 Properties	22
I.5 Background	24
II. EXPERIMENTAL PROCEDURE	29
II.1 Alloy Preparation	29
II.2 Technique of Microstructural Characterization	36
III. RESULTS AND DISCUSSION	41
III.1 Schaeffler Type Diagram for Fe-Al-Mn-Ni Weld Metal	47
III.2 Development of a Martensite Start Equation	52
III.3 Ferrite Transformations	59
IV. CONCLUSIONS	65
V. REFERENCES	66

LIST OF FIGURES

	<u>Page</u>
Figure 1. Historical trends in the relative importance of chromium usage in metallurgical, chemical and refractory applications (1).	7
Figure 2. Distribution of oxide phases with composition for oxidation of Fe-Ni-Al alloys at 800°C in pure oxygen (3).	9
Figure 3. Oxide map for the Fe-Mn-Al system at 800°C; full lines represent phase boundaries and the dashed lines represent regions with similar scale morphologies (4).	11
Figure 4. A compilation of the weight gain data after nine hours reaction in a gas mixture of hydrogen plus one volume percent hydrogen sulphide (5).	14
Figure 5. Phase diagram for the Fe-Mn-Al system proposed by Koster and Tonn (8).	16
Figure 6. Isothermal section for the Fe-Mn-Al ternary system at 760°C showing the extent of the beta manganese phase (9).	18
Figure 7. Isothermal section for the Fe-Mn-Al system at 950°C (13).	20
Figure 8. Vertical sections parallel to the Fe-Al system for varying nickel concentrations (14).	21
Figure 9. Fe-Al binary phase diagram.	26
Figure 10. Combined effects of alloy elements. Increasing amounts of austenite stabilizer (X) are observed to expand the gamma loop of a Fe-Y binary system.	28

LIST OF FIGURES (Continued)

	<u>Page</u>
Figure 11. Schematic of the weld metal preparation procedure.	31
Figure 12. Temperature factor $\exp(-2M)$ of iron at 20°C as a function of $(\sin \theta)/\lambda$ (24).	40
Figure 13. Effect of increasing aluminum content for weld metal having a nickel equivalent of 20. a) 1.5 wt% Al b) 5.0 wt% Al c) 7.0 wt% Al.	42
Figure 14. Effect of increasing nickel equivalent for weld metal containing 1.5 weight percent aluminum. 1) 20 b) 30 c) 70.	43
Figure 15. Microstructure of weld metal containing 6 wt% aluminum and a nickel equivalent of 32. Austenite and "delta type" ferrite are observed.	45
Figure 16. The Schaeffler diagram for weld metal microstructure.	46
Figure 17. "Schaeffler-type" diagram for Fe-Al-Mn-Ni weldments.	48
Figure 18. Dilatometric curve for a 1.5 wt% Al - 32 Ni _{eq} alloy cooled from 800°C . The epsilon _{eq} start (ϵ_s) and α' -martensite start (M_s) temperatures are indicated.	50
Figure 19. Hypothetical paths for the formation of α' martensite from austenite (33).	53
Figure 20. Martensite start line superimposed on the Schaeffler diagram for Fe-Mn-Ni-Al weld metal.	56
Figure 21. Isopleth used to predict phase transformations in Fe-Al-Mn-Ni weld metal.	60

LIST OF TABLES

		<u>Page</u>
Table I.	World Chromium Ore Resources (1).	2
Table II.	U.S. Chromium Imports from Various Sources (1).	3
Table III.	Prospects for Chromium Savings by Material Substitution and Redesign (1).	5
Table IV.	Base Plate Composition.	30
Table V.	Composition (weight percent)/Micro-structure Results for Fe-Al-Mn-Ni Weld Metal.	33
Table VI.	Martensitic Start Data for Various Weld Metal Compositions (weight percent).	55
Table VII.	Chromium Equivalent Coefficients for Aluminum.	58
Table VIII.	High Temperature X-Ray Diffraction Results for Weld Metal Containing 6 wt% Al with a Nickel Equivalent of 32.	62
Table IX.	Analytical Compositions (weight percent) for Weld Metal Containing 6 wt% Al with a Nickel Equivalent of 32.	64

ACKNOWLEDGEMENTS

I would like to acknowledge the United States Department of Energy for the research support. My special thanks to Dr. David LeRoy Olson for his advice and encouragement throughout the course of this investigation. I would like to extend my acknowledgement to Dr. David K. Matlock and Dr. William D. Copeland and Ray Dixon as members of my graduate committee. My appreciation is due to Drs. G.R. Edwards and E. Brown for their valuable discussion and suggestions. I am also indebted to my colleagues, C.E. Cross and J. Self for their assistance and advice. I wish to thank Bill Hutchinson (LANL) for performing the EDS analysis.

I. INTRODUCTION

I.1 Strategic Significance

Currently all the chromium used in the United States is imported. The most plentiful resources are in South Africa and Rhodesia. About 95 percent of the world reserves are located in these two countries (Table I). A review on the "Contingency Plans for Chromium Utilization" published by the National Materials Advisory Board (NMAB) of the National Academy of Sciences (1) makes our vulnerability regarding the chromium situation well known. NMAB reports that in the past the United States has imported chromium from several geographic locations. These sources are reported in Table II. However, it is estimated that these secondary sources may soon become exhausted. Chromium deposits in the United States are extremely limited and no prospects exist for the discovery of new reserves. According to the 1981 consumption rate the world will be completely dependent upon South Africa and Rhodesia for chromium within 25 to 75 years. In spite of this little has been done in terms of conservation or recycling.

Thirty-five percent of the total chromium usage is in essential applications (1). These applications include high strength steels, high temperature materials and corrosion-

Table I. World Chromium Ore Resources (1)

Country	Known Ore Reserves		Known Potential Ore	
	Million Short Tons Ore	%World	Million Short Tons Ore	%World
South Africa	1,194	62.4	2,333	76.5
Rhodesia	626	32.7	626	20.5
USSR	24	1.2	25	0.8
Philippines	5	0.3	< 1	< 0.05
Turkey	2	0.1	6	0.2
All other	<u>63</u>	<u>3.3</u>	<u>58</u>	<u>2.0</u>
TOTAL	1,914	100.0	3,049	100.0

Table II. U.S. Chromium Imports from Various Sources, 1963-1976 (1,000 short tons) (1)

Year	USSR	Turkey	South Africa	Rhodesia	Philippines	Other	Total
1963	64	25	186	89	47	23	434
1964	103	32	134	110	51	29	459
1965	91	51	163	110	61	29	505
1966	112	59	280	65	77	48	641
1967	113	35	164	49	43	23	427
1968	125	49	147	--	38	23	382
1969	118	56	141	--	44	24	383
1970	170	79	137	--	48	35	469
1971	112	107	141	8	36	27	431
1972	154	40	109	40	29	59	431
1973	82	41	126	51	44	44	388
1974	103	40	142	47	58	42	432
1975	120	53	147	101	48	111	580
1976	61	61	172	67	37	101	499

resisting alloys commonly applied in the manufacture of jet engines, petrochemical and power plant equipment, and other critical products (1). The remaining 65 percent is used in non-essential applications. Table III shows the distribution of chromium usage and the potential savings in several applications. According to the data in Table III it is technically feasible to replace 26 percent of the total chromium almost immediately. Another 40 percent can be saved after ten years of research and development.

Figure 1 shows the historical trends of chromium usage. On the average 65 percent is used in metallurgical applications. The stainless steel industry accounts for a majority of this usage. Therefore conservation and substitution in this area will provide the maximum savings in terms of tonnage. The fear of a chromium embargo and the strategic significance of the element has prompted the search for alternatives to austenitic stainless steels. Most austenitic stainless steel consists of over 16 weight percent chromium. These alternatives will use elements which promote the formation of tenacious oxide films (i.e. Al, Si) and other alloy elements (i.e. Ni, Mn, C, N) which tend to stabilize the FCC austenitic crystal structure of iron.

The purpose of this investigation is to find an alternative to stainless steel filler materials. Specifically the

Table III. Prospects for Chromium Savings by Materials Substitution and Redesign
(1,000 short tons)

End Use	Consumption Forecast for 1977	Potential Chromium Savings	
		Category 1 ^a	Category 2 ^b
<u>Metallurgical</u>			
Wrought stainless and heat-resisting steels	232	69.6 (30%) ^c	69.6 (30%)
Tool steels	6	0 (0%)	
Wrought alloy steels	43	6.5 (15%)	30 (70%)
Cast alloy steels	14	1.4 (10%)	8.4 (60%)
Alloy cast irons	8	0.8 (10%)	4.8 (60%)
Nonferrous alloys	14	0 (0%)	0.7 (5%)
Other	6	1.8 (10%)	1.8 (50%)
Subtotal	<u>323</u>	<u>80.1</u> (24.8%)	<u>115.3</u> (35.7%)
<u>Refractories</u>			
Chrome and chrome- magnesite brick	10	7.5 (75%)	2.5 (25%)
Magnesite-chrome brick	14	4.0 (28%)	8.0 (56%)
Granular chrome-bearing materials	27	5.0 (18.5%)	20.0 (74%)
Granular chromite	10	4.0 (40%)	4.0 (40%)
Subtotal	<u>61</u>	<u>20.5</u> (33.6%)	<u>34.5</u> (56.6%)

Table III. Prospects for Chromium Savings by Materials Substitution and Redesign
(1,000 short tons) (Continued)

End Use	Consumption Forecast for 1977	Potential Chromium Savings	
		Category 1 ^a	Category 2 ^b
<u>Chemicals</u>			
Pigments	18	4.5 (25%)	9.0 (50%)
Metal finishing	15	7.5 (50%)	2.3 (15%)
Leather tanning	11	0 (0%)	11.0 (100%)
Drilling muds	3	0 (0%)	0 (0%)
Wood treatment	4	2.0 (50%)	2.0 (50%)
Water treatment	4	0 (0%)	2.0 (50%)
Chemical manufacture	5	0 (0%)	2.5 (50%)
Textiles	2	1.0 (50%)	2.0 (50%)
Catalysts	< 1	0 (0%)	0 (0%)
Other	5	1.0 (20%)	3.0 (60%)
Subtotal	<u>68</u>	<u>16.0 (23.5%)</u>	<u>32.8 (48.2%)</u>

^a Technically feasible now.^b Potentially feasible after 10 years of research and development.^c Number in parentheses indicates percent saving of consumption forecast for each end use category.^d Percent saving of total for all categories.

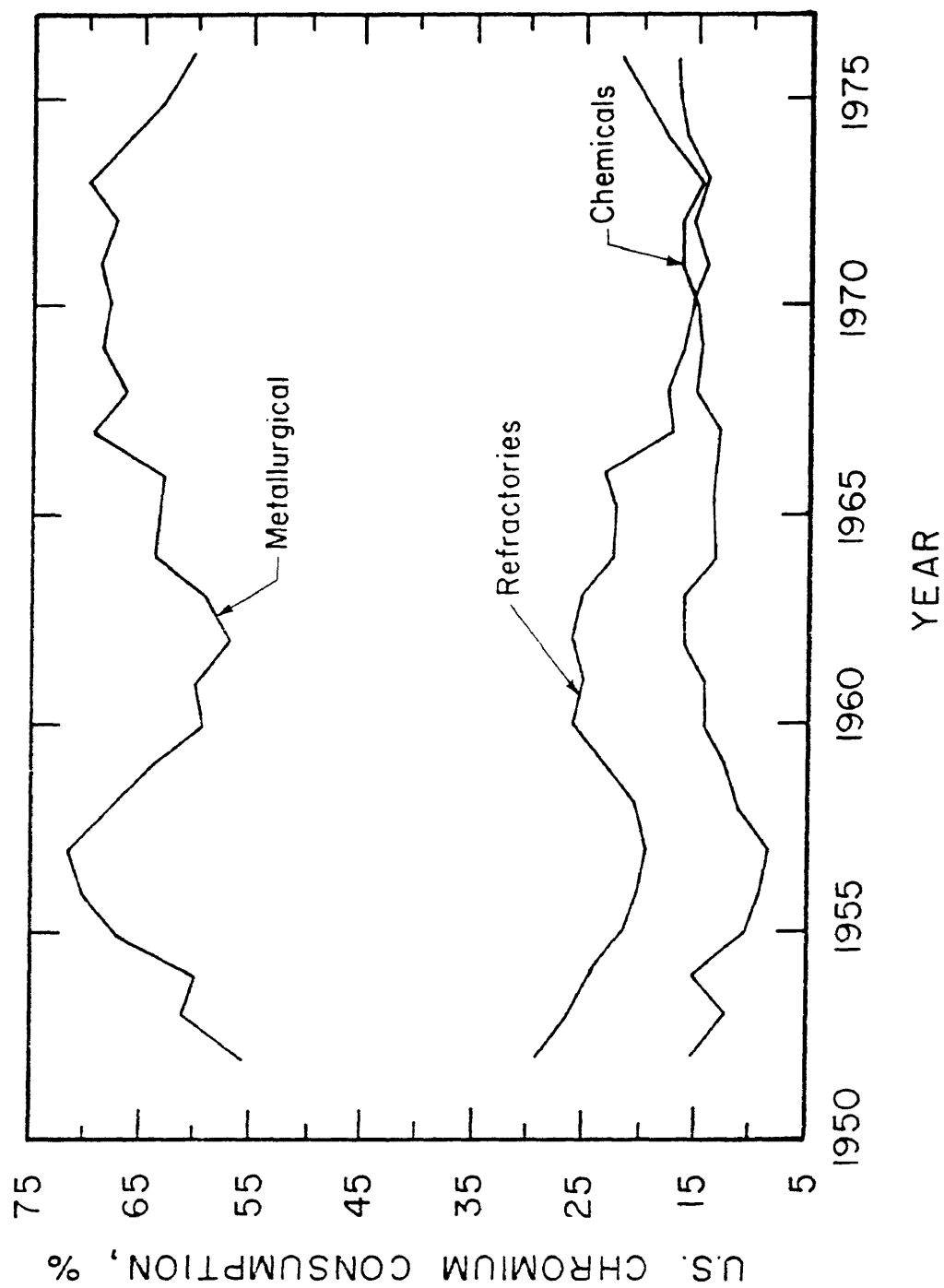


Figure 1. Historical trends in the relative importance of chromium usage in metallurgical, chemical and refractory applications (1).

weldability of the Fe-Al-Mn-Ni alloy system has been evaluated.

I.2 Oxidation/Sulfidation Behavior

Tomaszewiaz and Wallwork (2) have investigated the oxidation behavior of iron-aluminum alloys containing either nickel or manganese. The addition of nickel and aluminum to Fe-Al-Ni ternary alloys were found to be incompatible. That is while aluminum was found to promote Al_2O_3 scale formation, nickel promoted the formation of bulky iron oxide nodules. An oxide map (3) prepared at 800°C for 24 hour oxidation in pure oxygen (200 torr) is presented in Figure 2. Oxidation behavior has been categorized based on alloy composition. Group I alloys found thick scales of iron oxide. Alumina scales covered alloy surfaces in group II materials. These scales formed in conjunction with iron oxide nodules. Alloys having compositions greater than ten weight percent aluminum are classified as group III. These alloys formed thin Al_2O_3 type scales with little evidence of Fe_2O_3 formation. The absence of Fe_2O_3 in the scale is known to significantly improve oxidation resistance. In summary Fe-Al-Ni alloys containing less than ten weight percent aluminum have insufficient aluminum to form a protective Al_2O_3 scale. This is slightly higher than the seven weight percent aluminum

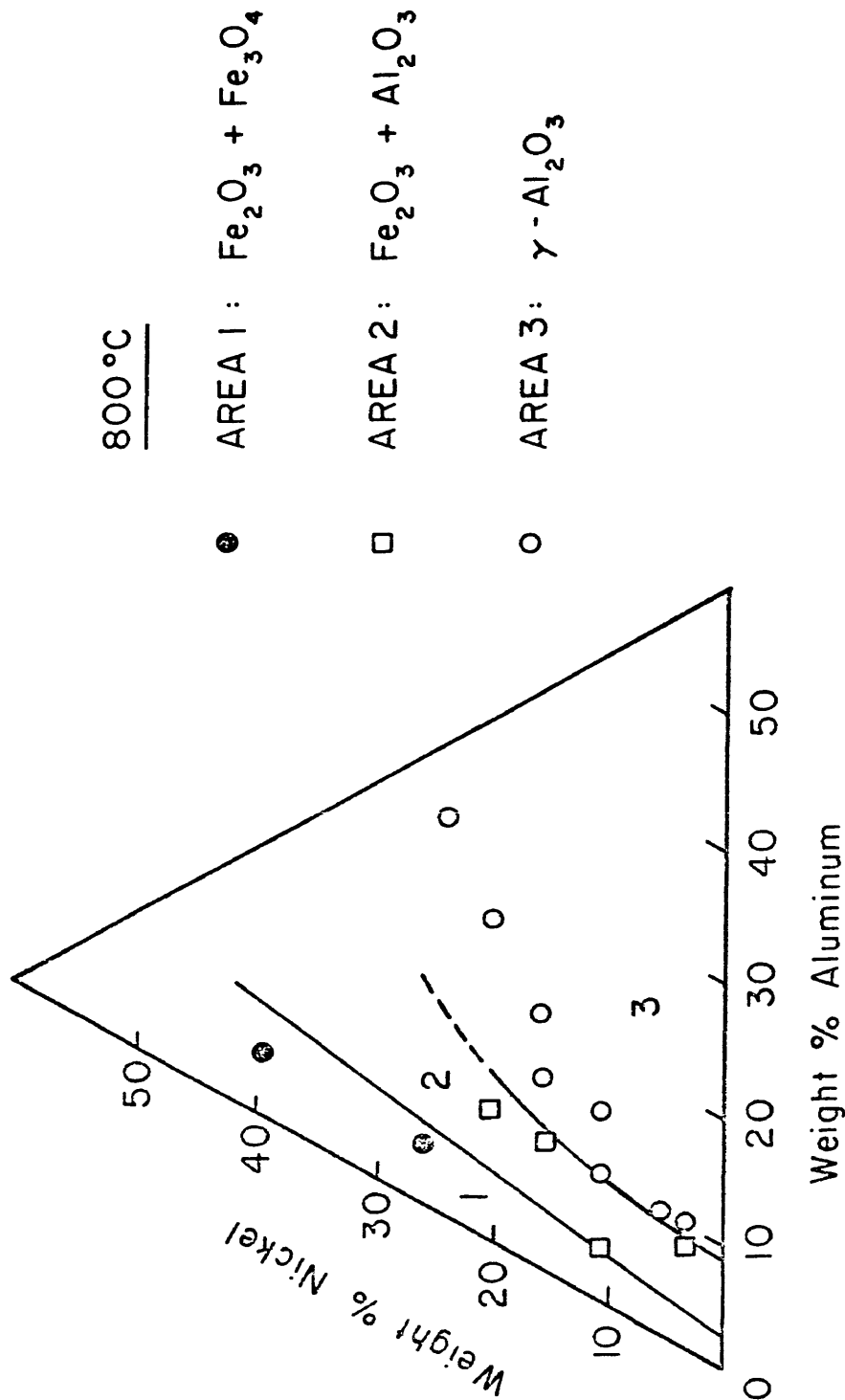


Figure 2. Distribution of oxide phases with composition for oxidation of Fe-Ni-Al alloys at 800°C in pure oxygen (3).

required for "good" oxidation resistance at 800°C for binary iron-aluminum alloys.

An oxide mapping technique was employed by Jackson and Wallwork (4) to characterize the oxidation behavior of Fe-Mn-Al alloys. These results are presented in Figure 3. Alloys were classified into four major types according to morphology and the composition of the scale produced. These are as follows:

Type I: Alloys which contain six to seven weight percent aluminum and less than eight weight percent manganese. Microstructurally these alloys are ferritic. Oxidation resistance was poor due to the formation of non-protective Fe_2O_3 scales.

Type II: Alloys are duplex austenite and ferrite, containing five to ten weight percent aluminum and greater than eight weight percent manganese. The duplex microstructure makes the corrosion characteristics complex. In general, oxidation resistance was poor but varied with percentage of austenite and ferrite. Alloys with higher aluminum concentrations contained more ferrite. Scales which formed on this phase were of the protective Al_2O_3 type. A much bulkier scale consisting

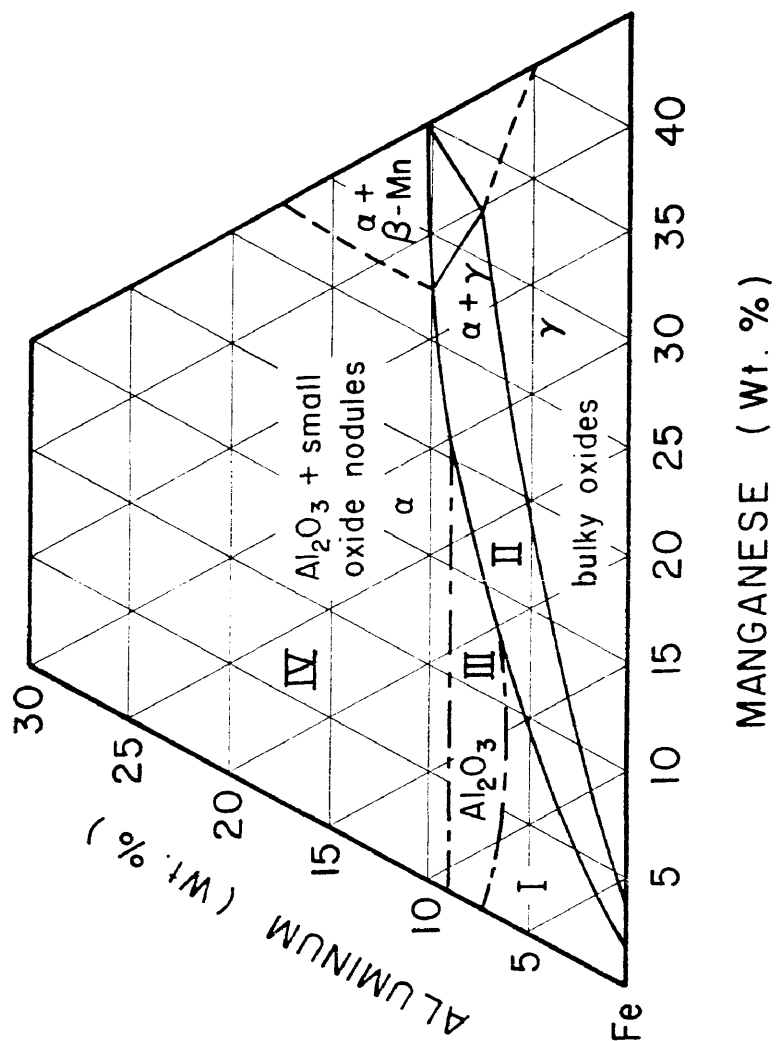


Figure 3. Oxide map for the Fe-Mn-Al system at 800°C; full lines represent phase boundaries and the dashed lines represent regions with similar scale morphologies (4).

of iron and manganese nodules was found to form on the austenitic phase. Reducing aluminum concentrations raised the percentage of austenite. Consequently more extensive bulky oxide formation was observed.

Type III: These alloys are ferritic containing six to nine weight percent aluminum and less than twenty weight percent manganese. Characterized by the formation of thin adherent alumina scales these alloys were the most resistant to oxidation.

Type IV: Again these alloys are ferritic containing in excess of nine weight percent aluminum. Type IV alloys also formed protective Al_2O_3 scales but oxidation resistance was poor as a result of scale spallation.

Fe-Mn-Al alloys require high manganese additions to remain austenitic but upon exposure to oxidizing environments these form non-protective scales. Ferritic alloys with less than ten weight percent manganese form protective alumina scales and as such have good oxidation resistance. Duplex alloys are expected to fall somewhere between the poor oxidation of the austenite and that of the totally ferritic alloy. In terms of having an Fe-Mn-Al alloy that is equivalent to

austenitic stainless steels it appears that the limitations of a ferritic alloy are too restrictive to allow economical production of necessary product shapes. Alternatively an austenitic alloy could be prepared and then the surface chemistry adjusted (i.e. remove Mn) so that it falls within the composition of type III alloys.

Tomas (5) has investigated the sulfication resistance of Fe-Nb, 3XX stainless steels and Fe-Mn-Al alloys. These alloys were tested in a reducing atmosphere of $H_2 + 1 \text{ vol.}\%$ H_2S for nine hours at 700°C and 800°C . The weight gain data of these tests are presented in Figure 4. The most resistant materials contained five weight percent aluminum (Fenbal 7) or seventeen weight percent niobium (Fenbal 17). Femnal 30 (Fe - 30.4 Mn, 7.6 Al, 0.8 C) and a similar silicon bearing alloy #11-10-4B (Fe - 30.5 Mn, 8.4 Al, 1.5 Si, 1.05 C) also showed good performance.

Perkins (6) has systematically studied the oxidation of Fe-Mn-Al alloys. His results show that alloys containing 3 to 15 weight percent aluminum and 0 to 40 weight percent manganese had no resistance to oxidation/sulfidation at 982°C and displayed large weight losses with the introduction of interstitial elements.

Wang and Beck (7) investigated Fe-30Mn-10Al-1Si alloys as an alternative to brass for ship propellers. Micro-

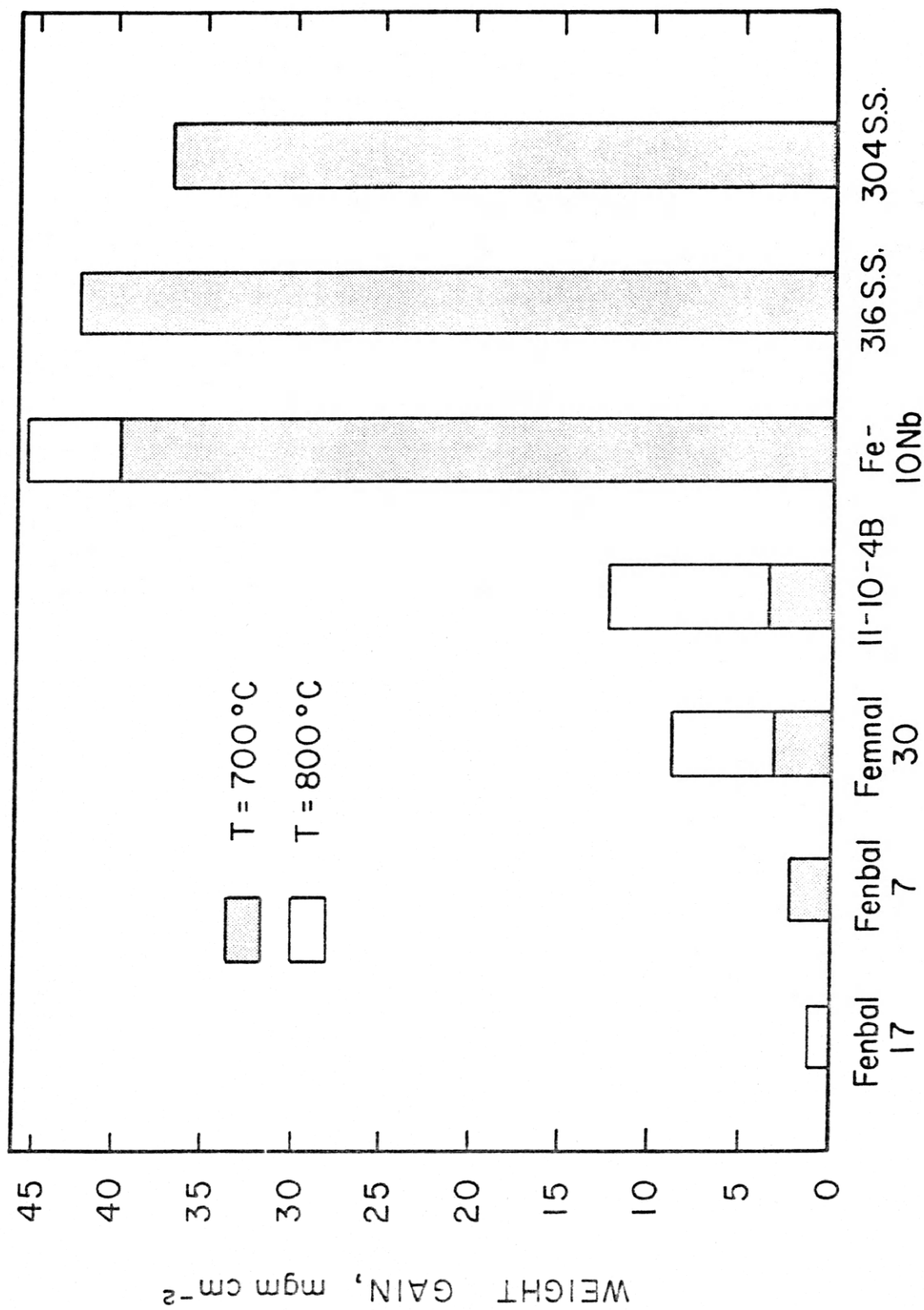


Figure 4. A compilation of the weight gain data after nine hours reaction in a gas mixture of hydrogen plus one volume percent hydrogen sulphide (5).

structurally the Fe-Mn-Al-Si alloy has an austenitic matrix but also contains a small percentage of ferrite in the as cast condition. The small amounts of delta ferrite may be significant in reducing hot cracking susceptibility. The alloy was exposed to natural seawater for 768 hours and showed no evidence of corrosion. A stainless steel (0.08C, 18.59Cr, 9.63Ni, 1.07Ti) subjected to the same environment showed slight signs of rusting. This stainless steel was reported to have corrosion resistance superior to that of manganese-iron brass used in marine type environments.

I.3 Phase Diagrams

Fe-Mn-Al Ternary System

The iron-aluminum system consists of an extensive ferritic terminal solid solution extending to 34 weight percent aluminum. In contrast the iron-manganese system has a broad region of stable austenite. At some combination of aluminum and manganese in iron a two phase field of austenite and ferrite must exist. Koster and Tonn (8) have located the boundaries of the two phase field using metallographic and dilatometric techniques. Their results reproduced in Figure 5 indicate stable austenite up to 20 weight percent aluminum and 50.0 weight percent manganese. Austenitic, high aluminum-manganese alloys were found to be unstable and

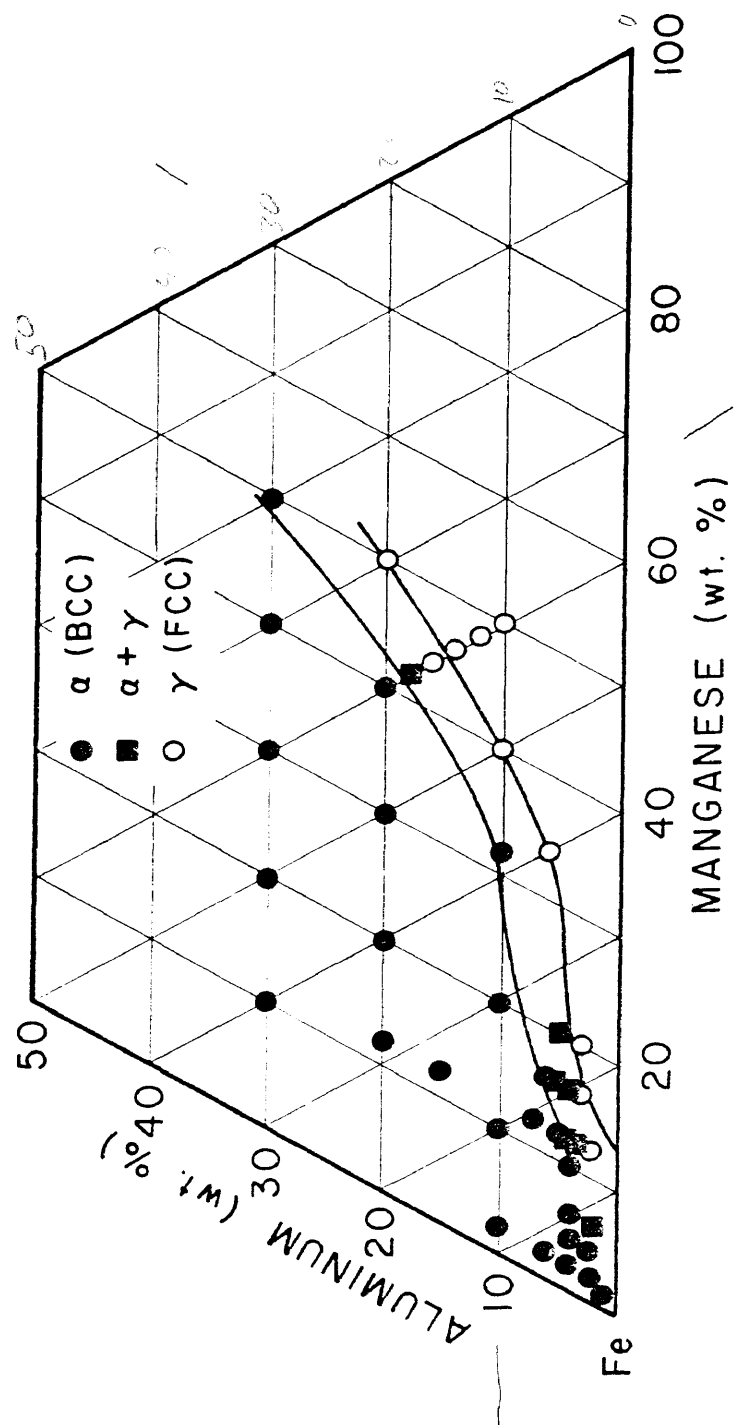


Figure 5. Phase diagram for the Fe-Mn-Al system proposed by Koster and Tonn (8).

transformed to beta manganese on cooling. No indication of the temperature or composition dependence of the transformation was made nor has it been included in their proposed phase diagram. Schmatz (9) examined alloys containing 5 to 20 weight percent aluminum and 5 to 67 weight percent manganese. Metallographic analysis provided a confirmation of the $(\alpha+\gamma)/\gamma$ boundary determined by Koster and Tonn. A three phase field was found to exist at a composition of 10 weight percent aluminum and 35 weight percent manganese. Ferrite and austenite coexist with a third phase having a beta manganese crystal structure. These phase fields are indicated in the ternary isothermal section shown in Figure 6. Schmatz (9) reports that the three phase region shifts to slightly higher aluminum and much higher manganese contents with increasing temperature. Also the composition ranges of the two phase fields, $\alpha+\gamma$ and $\gamma+\beta$ contract with increasing temperature.

Fe-Ni-Al Ternary System

The Fe-Ni-Al ternary was investigated by Koster (10) as early as 1933. Koster established by means of thermal, microscopic and magnetic analysis the liquidus surface of this ternary system and the ranges of the alpha and gamma alloys in this system. Widening of the $\gamma+\alpha$ miscibility gap

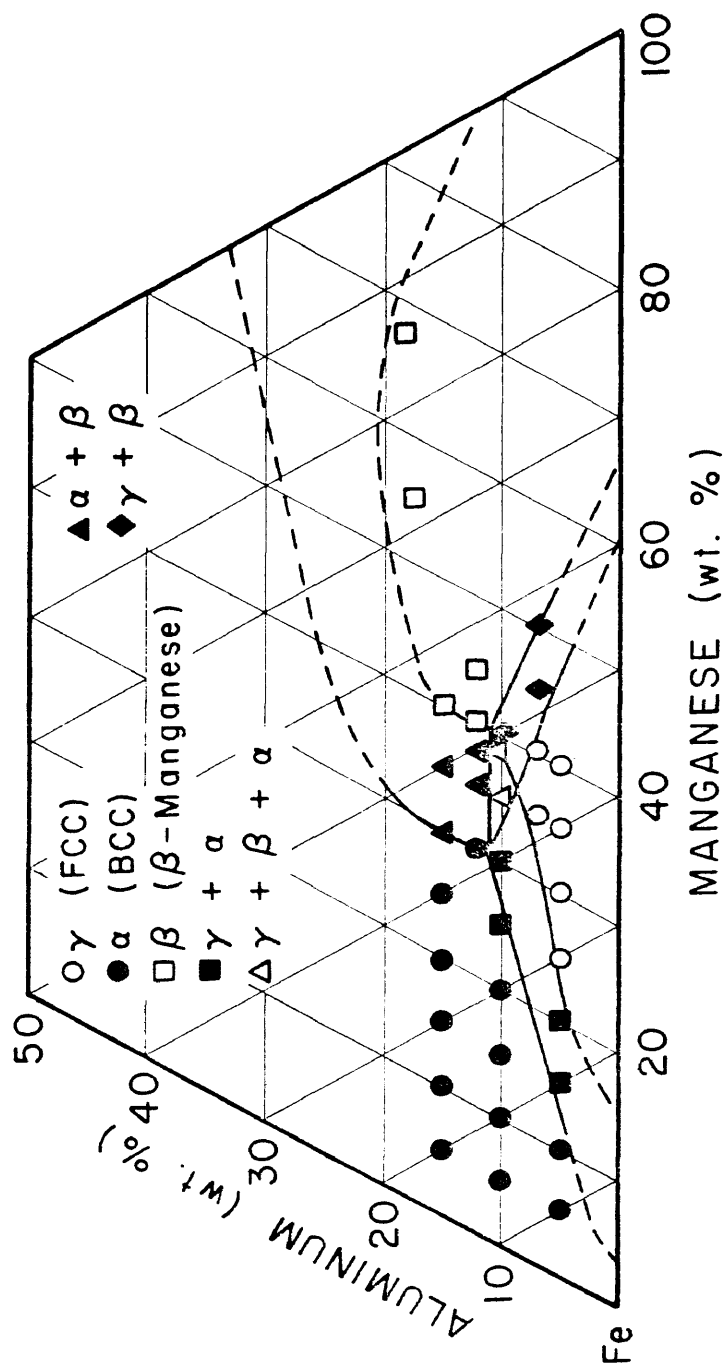


Figure 6. Isothermal section for the Fe-Mn-Al ternary system at 760°C showing the extent of the beta manganese phase (9).

between γ (fcc) and α (bcc) phase fields was observed to take place with decreasing temperature. At the melting temperature the two phase gap is closed by either a eutectic or peritectic reaction. The peritectic is derived from the Fe-Ni system and the eutectic is thought to be associated with the Ni-Al system.

Using x-rays Bradley (11) discovered that body-centered cubic alloys develop a two phase $\alpha+\alpha'$ field. α denotes a BCC crystall structure without order, α' is an ordered phase of NiAl or FeAl type (aluminum at the cube corners). This reaction is reported as being the cause of the high coercivity in permanent-magnetic alloys (12). The phase diagram is further complicated by the decomposition of FCC alloys into γ and γ' where γ is disordered and γ' is an ordered phase of the Ni_3Al or Ni_3Fe type (nickel at the center of cube faces). Bradley has shown that "two phase" miscibility gap which was reported by Koster is actually comprised for five separate positions. Three two phase areas separated by two three phase areas. These are $\gamma+\alpha$, $\gamma+\alpha+\alpha'$, $\gamma+\gamma'+\alpha$ and $\gamma+\alpha'$. The 950°C isothermal section (13) in Figure 7 illustrates these fields and also shows the extent of the single phase γ and α fields.

Isothermal sections have been used to generate a series of isopleths parallel to the Fe-Al system from the melting point down to 750°C (14). These are presented in Figure 8.

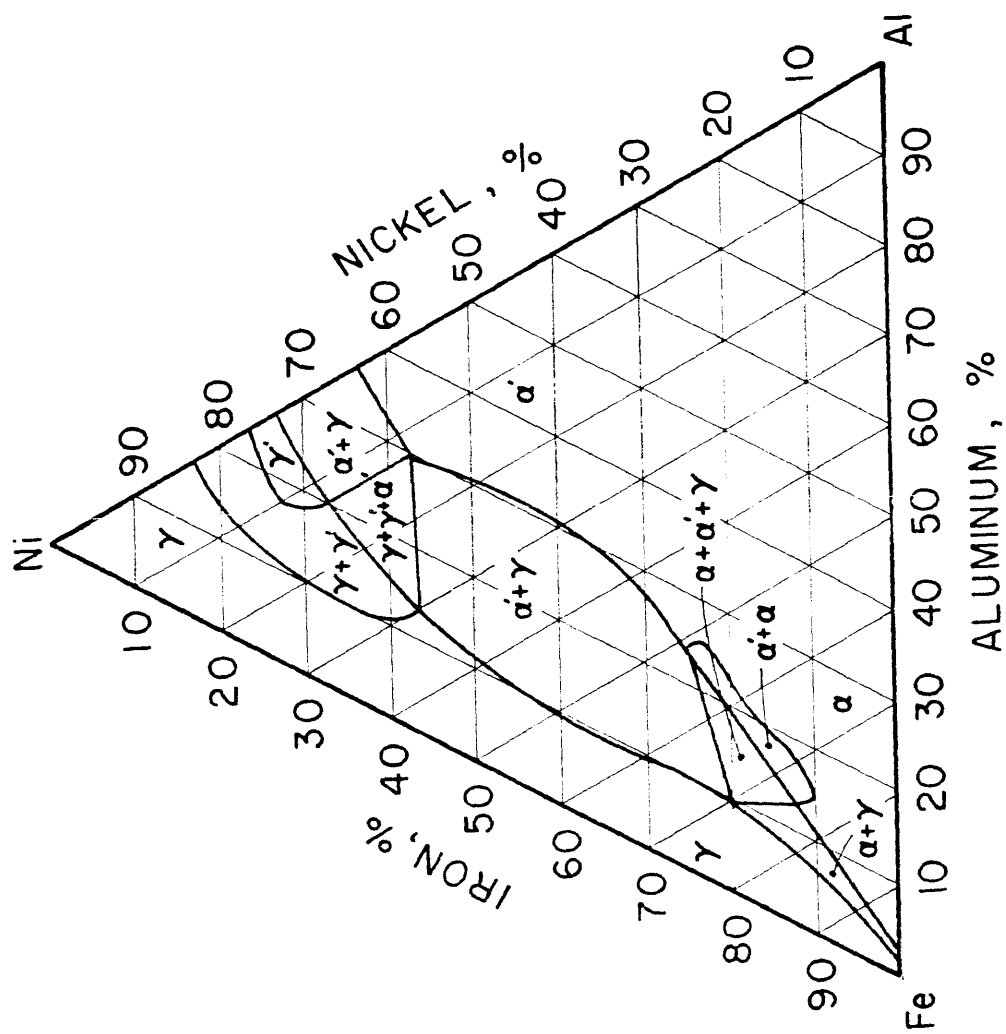


Figure 7. Isothermal section for the Fe-Mn-Al system at 950°C (13).

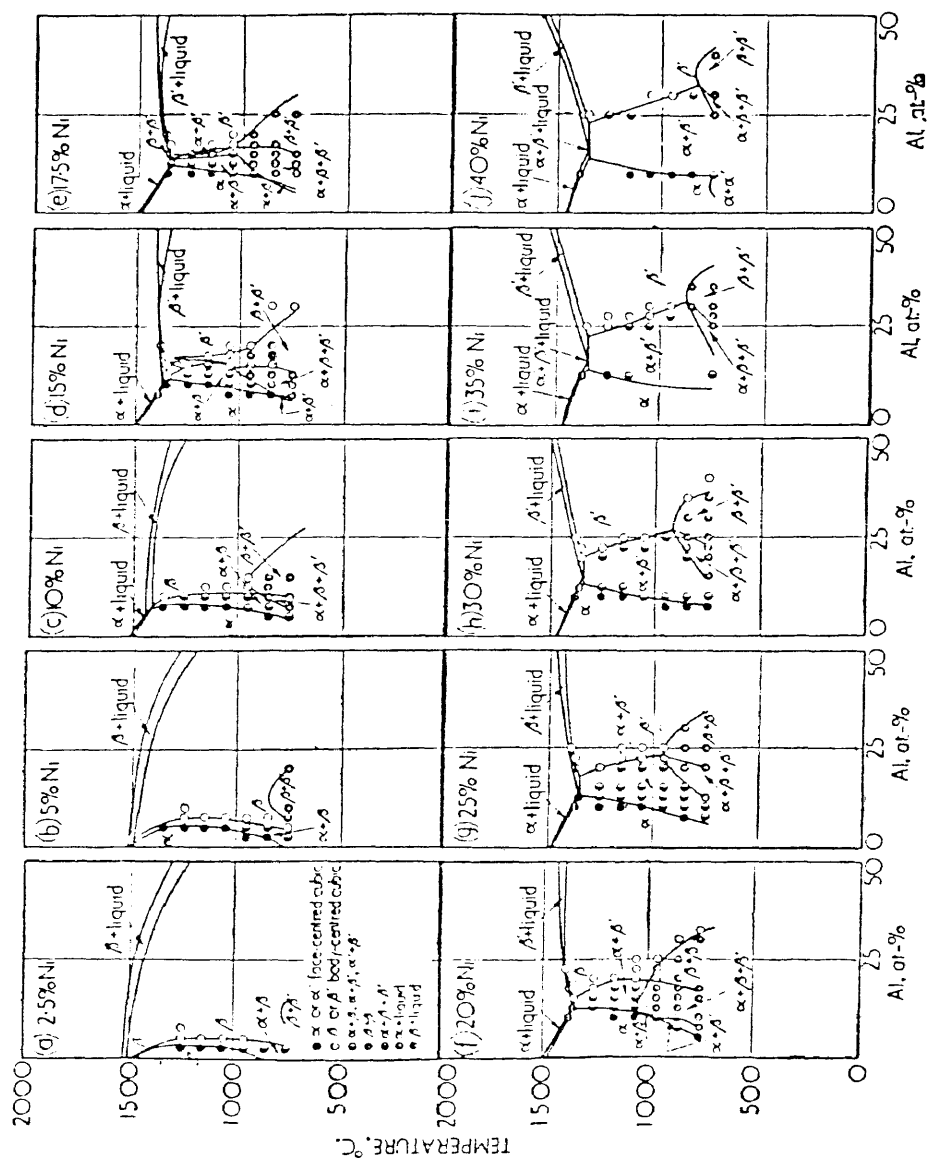


Figure 8. Vertical sections parallel to the Fe-Al system for varying nickel concentrations (14).

Increasing nickel content is observed to expand the γ phase field. A gradual enlargement of the $\gamma+\alpha$ field occurs as well. The extent of the γ phase approaches a maximum of 17.5 atomic percent nickel, 12.5 atomic percent aluminum balance iron at 1340°C. The peritectic reaction $L+\alpha=\gamma$ is observed at ten weight percent aluminum in the ten weight percent nickel section (Figure 8c). At 25 weight percent nickel the liquidus and solidus curves fall to a minimum at 13 weight percent aluminum as shown in Figure 7g. This corresponds to the trough of the eutectic valley, liquid + $\gamma+\alpha'$. The transitional sections (Figure 8d to 8f) consisting of 15 to 20 weight percent nickel are self-explanatory. It is interesting to note the disappearance of α and the existence of two separate $\gamma+\alpha'$ phase fields. The $\alpha+\alpha'$ miscibility gap is observed to develop a narrow wedge extending to the melting point. This gives rise to four phase equilibria of the type $L+\gamma+\alpha+\alpha'$ at the melt in the 17.5 weight percent nickel section.

I.4 Properties

Schmatz (15) has investigated iron-based alloys containing aluminum, manganese and carbon with emphasis on obtaining an austenitic microstructure and mechanical properties equivalent to stainless steel. A range of compo-

sitions were found which nearly met these requirements. Minor additions of silicon were found to improve both strength and oxidation resistance. One promising alloy contained Fe-8Al-30Mn-1C-1.5Si. Its strength exceeded commercial stainless steels at room temperature and was increased both by quench aging and strain aging. At 650°C a tensile strength of 100,000 psi was attained with an elongation of five percent. High aluminum and manganese alloys embrittled due to beta manganese formation. Schmatz also reports that aluminum concentrations greater than five percent impair austenite stability. Charles and Berghezan (16) investigated the influence of carbon and aluminum additions on the mechanical properties under uniaxial tensile loading and by Charpy V notch impact tests at room temperature and -196°C of Fe-24Mn alloys. It was concluded that a Fe-24Mn-5Al-0.2C alloy had potential for use in cryogenic applications. Additions of aluminum and carbon were found to contribute to the stability of the austenite phase by suppressing the γ - ϵ martensitic transformation of the binary Fe-24Mn alloy and to the solution hardening of the manganese-rich austenitic alloy.

Schumann (17, 18), and Holden, Bolton and Petty (19) have determined that binary Fe-Mn alloys containing 28 to 50 percent manganese possess stable austenites when cooled to

room temperature. For manganese contents between 15 and 28 percent there exists a two-phase region of austenite plus hexagonal epsilon martensite. Still lower manganese contents (less than 15 percent) the austenite transforms partially into tetragonal α' martensite responsible for the sharp decrease in toughness at low temperature.

I.5 Background

Chromium additions to ferrous alloys are responsible for the superior oxidation resistance through the ability to provide a protective oxide layer. Examination of the Fe-Cr binary system reveals the presence of a closed gamma loop extending to a maximum of twelve weight percent chromium. Higher concentrations increase the stability of the BCC phase of iron, making chromium a ferrite stabilizer. A substitute for chromium must possess the ability to form a similar protective oxide layer. Aluminum has such an ability and is a non-strategic element. Tomaszewica and Wallwork (2) report that a minimum of seven weight percent aluminum is required in Fe-Al binary materials to endow them with oxidation/corrosion resistant properties equivalent to stainless steels. Iron-aluminum alloys have received little attention however due to the limitations of their ferritic microstructures. Like chromium, aluminum is a ferrite stabilizer although it is

considerably more potent. Figure 9 shows that the gamma loop of the Fe-Al binary system extends to a maximum of 0.63 weight percent aluminum. From 0.63 to 35 weight percent aluminum the alloys form a continuous series of ferritic solid solutions. In this field, order-disorder as well as magnetic to non-magnetic transformations are known to exist (20). Since no phase changes are involved in these transformations, the boundaries have been shown in the diagram as dashed and dotted lines. In contrast to the closed gamma field, Fe-Ni and Fe-Mn binary systems have broad regions of stable austenite. Thus, in the ternary system a closed gamma loop is forced to link up with an open gamma field.

A qualitative determination of the effects of alloying elements in iron solutions can be made by considering these elements to alter the stability of only the FCC and BCC phases of iron (i.e. change the boundaries of the austenite, austenite plus ferrite and ferrite phase fields). The basic type of binary equilibria with iron as one component were originally classified by Weaver (21) and later modified by Andrews (22) to account for anomalies. The Weaver scheme is the most straightforward as it classified alloy elements into two types - those which favor FCC iron, austenite stabilizers and those which favor BCC iron, the ferrite formers. These basic types are represented by the open γ -field of the Fe-Mn,

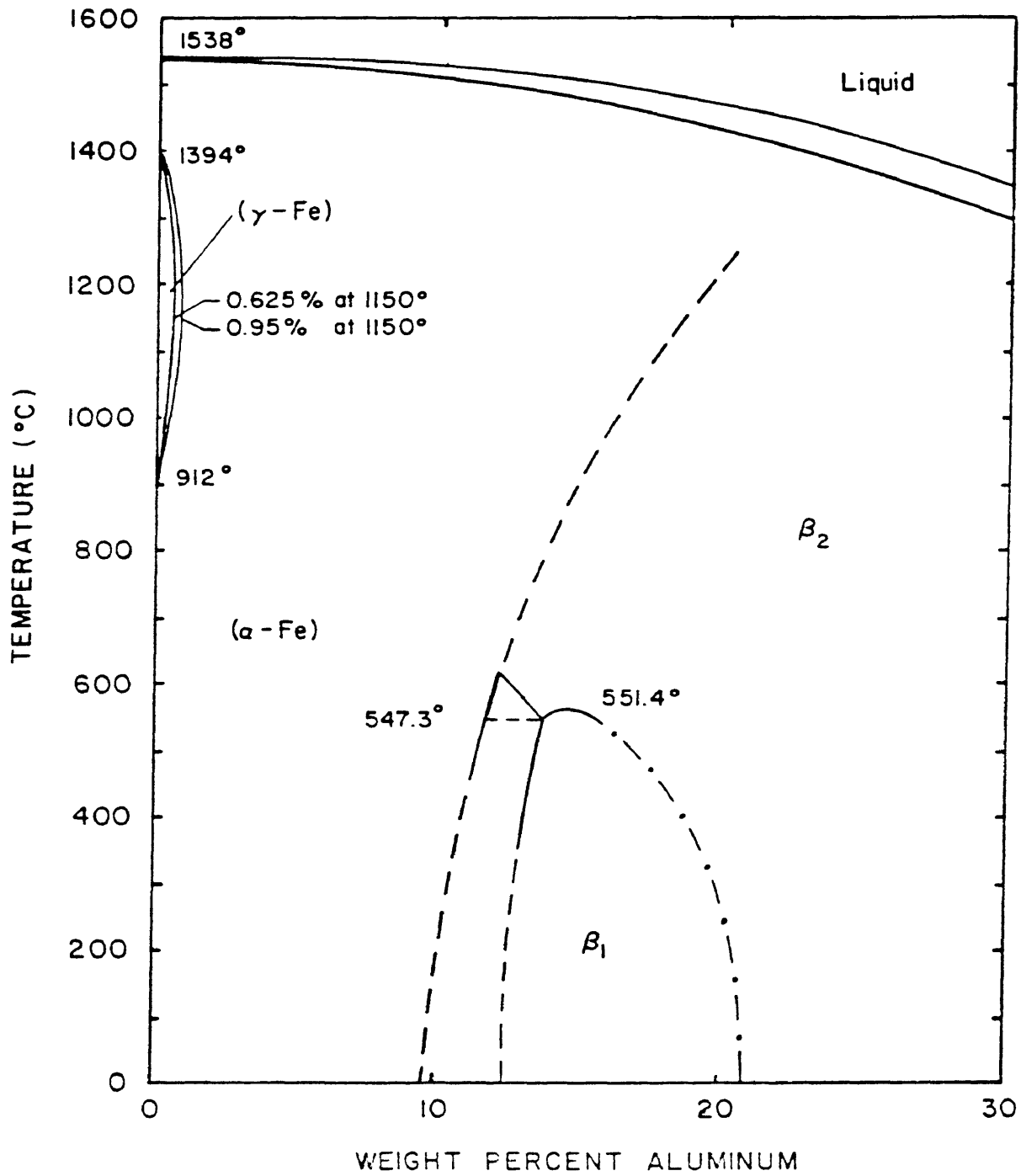


Figure 9. Fe-Al binary phase diagram.

Fe-Ni binary systems and the closed γ -loop of the Fe-Al binary.

If this classification scheme is valid then Fe-Al-Mn-Ni alloys are comprised of a single ferrite stabilizer (Al) and a summation of austenite stabilizer (Mn and Ni). If sufficient austenite stabilizer is added to Fe-Al binary alloys the gamma loop will expand to higher concentrations of aluminum. In order to obtain a corrosion resistant FCC alloy it is necessary to increase the solubility of aluminum in austenite to seven weight percent.

A design philosophy for Fe-Al-Mn-Ni alloys is summarized in Figure 10. A ternary system Fe-X-Y, where X is a summation of austenite stabilizers and Y is a summation of ferrite stabilizers is illustrated (23). The case of adding austenite formers X to a Fe-Y binary is considered. The solubility of increasing amounts of Y in the FCC phase of iron is observed to increase with increasing concentrations of austenite stabilizers.

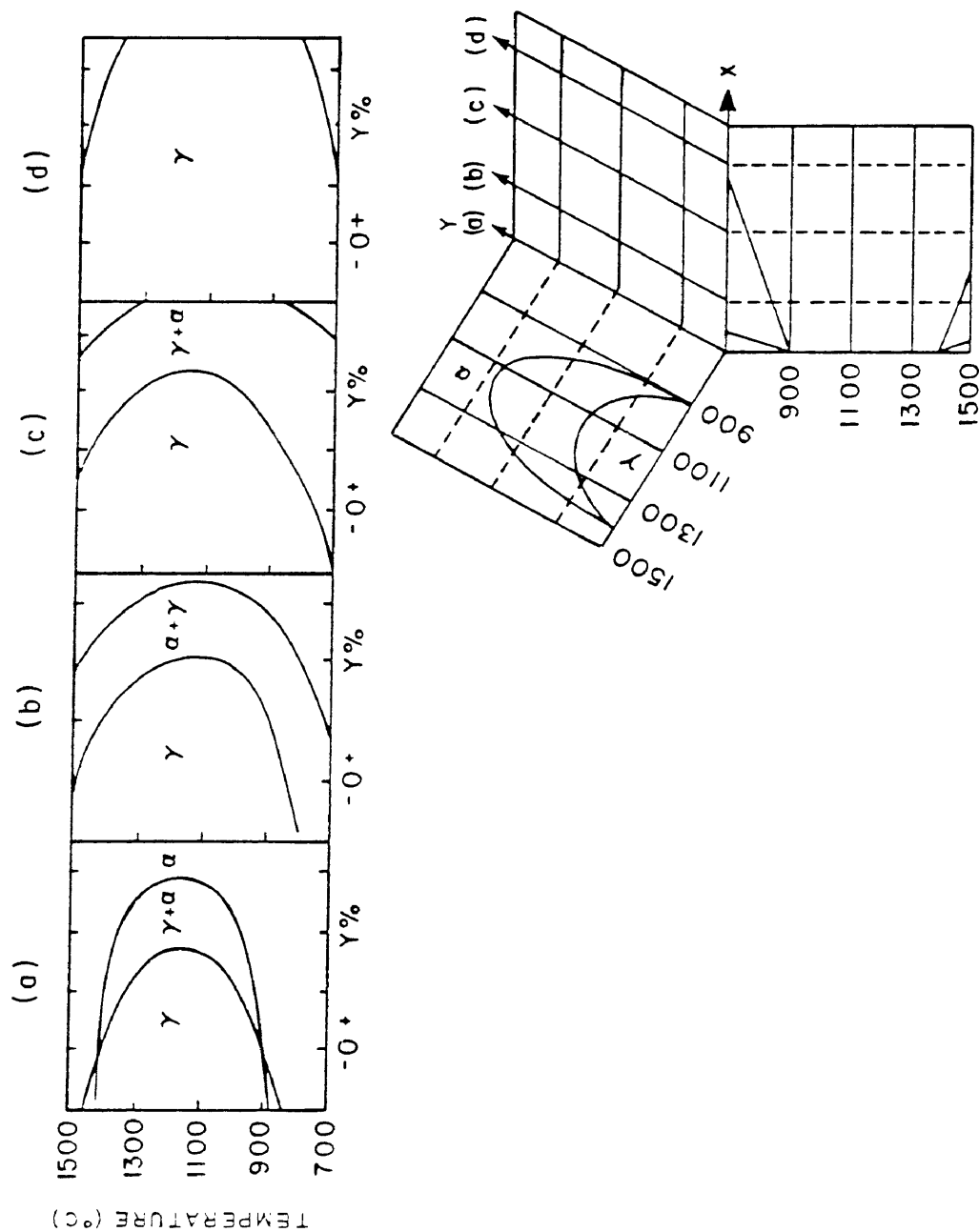


Figure 10. Combined effects of alloy elements. Increasing amounts of austenite stabilizer (X) are observed to expand the gamma loop of a Fe-Y binary system.

II. EXPERIMENTAL PROCEDURE

II.1 Alloy Preparation

The weld metal chemistries investigated varied from 0 to 8 weight percent aluminum, 0 to 35 weight percent manganese, 0 to 10 weight percent nickel with the balance iron. AISI 1018 steel (composition given in Table IV) was used as the parent material. The dimensions of the plates used for welding were 150mm by 35mm by 13mm (6 inches by 1 3/8 inches by 1/2 inches). A groove 0.8mm deep by 3.2mm wide (0.030 inches by 0.125 inches) was machined down the long axis of the plate according to Figure 11. Oxide was ground off the surface of each plate. The ground surface was then cleansed with acetone before welding. Reagent grade powders of aluminum, manganese, nickel and iron were uniformly mixed in various proportions and compacted in the groove under a 30,000 pound load. Several compactions were necessary in order for the groove to be filled flush with the surface of the plate. The intent of the compaction process is to reduce void space and to prevent arc pressure from dispersing the powders during welding.

The welding system consisted of a Hobart Cybertig-300 programmable constant current power supply used in conjunction with a traversing torch carriage of adjustable travel

TABLE IV. Base Plate Composition (in weight percent)

C	0.185	Ni	0.016
Mn	0.916	Cr	0.037
P	0.007	Si	0.037
S	0.014	Al	0.018

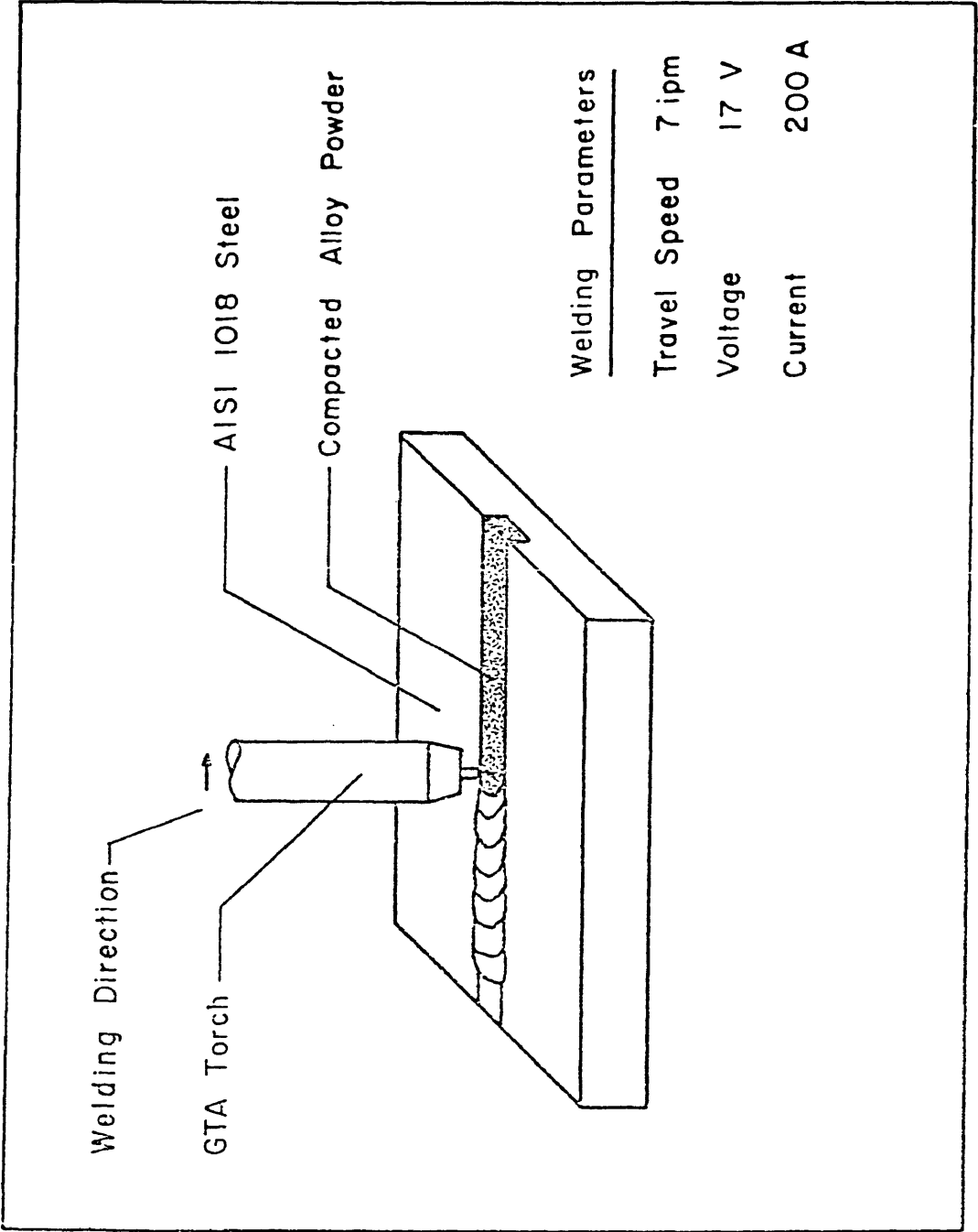


Figure 11. Schematic of the weld metal preparation procedure.

speed. Direct current, straight polarity gas tungsten arc (GTA) welding was used to produce single pass bead on plate weldments. The torch was allowed to travel down the center of the compacted powders at a rate of 3mm/sec (7 pim) as shown. Current and voltage were held constant at 200 amps and 17 volts respectively.

Heat input was calculated to be 1.2 KJ/mm (30 KJ/inch). Weldments were allowed to air cool. All welds were made using argon shielding and a 2.4mm (3/34 inches) tungsten - two pct thoria electrode with a 90⁰ included angle. The arc length was held constant at 2mm.

Metallographic sections taken down the centerline of the weldment and perpendicular to the travel direction showed that the dimensions of the fusion zone were larger than that of the groove indicating that all the powder had been melted along with some percentage of the parent material. Dilutions were found to be approximately 55 volume percent. Porosity was not observed in any of the metallographic sections. Compositions of the weldment wre analyzed from metallographic specimens utilizing emission spectroscopy. These results are given in Table V.

Table V. Composition/Microstructure Results for Fe-Al-Mn-Ni Weld Metal

Sample No.	C wt%	Mn wt%	Ni wt%	Al wt%	Microstructure
1	0.20	3.09	0.1	1.40	α'
2	0.20	3.77	0.10	4.26	$\alpha+\alpha'$
3	0.21	2.91	0.10	4.83	$\alpha+\alpha'$
4	0.18	6.30	0.10	1.35	α'
5	0.18	6.16	0.10	3.01	α'
6	0.20	5.68	0.10	7.04	α
7	0.14	9.50	0.10	1.99	α'
8	0.19	12.37	0.10	5.14	$\gamma+\alpha$
9	0.17	5.32	2.47	2.54	α'
10	0.17	3.97	4.93	1.57	α'
11	0.17	3.69	6.72	2.08	α'
12	0.19	2.79	1.72	2.86	α'
13	0.19	2.93	3.14	3.26	α'
14	0.19	2.99	5.68	3.14	α'
15	0.22	2.53	1.54	4.28	$\alpha+\alpha'$
16	0.21	2.67	3.22	4.09	$\alpha+\alpha'$
17	0.22	3.25	5.43	4.68	$\alpha+\alpha'$
18	0.16	5.94	1.47	1.65	α'
19	0.17	6.87	3.62	1.63	α'
20	0.19	5.57	4.80	1.61	α'
21	0.19	5.48	1.35	3.09	α'
22	0.19	5.39	2.71	2.74	α'
23	0.20	4.66	3.85	2.71	α'
24	0.20	6.38	3.09	4.99	$\alpha+\alpha'$
25	0.20	5.73	1.29	4.85	$\alpha+\alpha'$
26	0.18	8.64	1.64	1.60	α'
27	0.18	8.80	2.61	1.67	α'
28	0.19	6.83	3.64	1.36	α'
29	0.19	9.54	1.58	3.68	$\alpha'+\gamma$
30	0.17	9.13	3.51	3.74	$\alpha'+\gamma$
31	0.21	8.31	3.85	3.11	$\alpha'+\gamma$
32	0.20	8.85	2.80	5.10	$\alpha'+\alpha$
33	0.21	10.68	4.54	6.08	$\gamma+\alpha$
34	0.24	5.27	0.10	0.68	α'
35	0.22	5.28	0.10	1.49	α'
36	0.24	3.33	0.10	1.09	α'
37	0.20	8.62	0.10	1.06	α'
38	0.22	6.42	0.10	1.32	α'
39	0.26	6.28	0.10	1.59	α'
40	0.24	4.10	0.10	0.47	α'

Table V. Composition/Microstructure Results for Fe-Al-Mn-Ni Weld Metal (Continued)

Sample No.	C wt%	Mn wt%	Ni wt%	Al wt%	Microstructure
41	0.22	4.47	0.10	0.89	α'
42	0.19	4.94	0.10	1.66	α'
43	0.18	4.92	0.10	0.55	α'
44	0.20	6.50	0.10	1.48	α'
45	0.17	7.17	0.10	2.56	α'
46	0.18	9.13	0.10	4.17	$\alpha+\alpha'$
47	0.21	8.17	0.10	3.77	α'
48	0.18	5.73	0.10	1.97	α'
49	0.17	3.81	1.83	2.39	α'
50	0.17	2.62	0.79	1.88	α'
51	0.17	3.70	2.33	0.55	α'
52	0.18	4.32	2.82	1.19	α'
53	0.18	5.33	3.31	2.34	α'
54	0.18	5.13	3.13	2.69	α'
55	0.18	8.41	7.88	2.33	$\gamma+\alpha'$
56	0.20	9.94	1.03	1.18	α'
57	0.18	9.35	2.26	1.30	α'
58	0.18	10.45	4.15	1.44	$\gamma+\epsilon+\alpha'$
59	0.18	5.53	6.88	2.12	$\alpha'+\gamma$
60	0.18	5.88	7.96	2.22	$\alpha'+\gamma$
61	0.20	7.94	1.66	2.51	$\alpha'+\gamma$
62	0.18	9.08	1.07	0.55	α'
63	0.18	5.79	1.29	1.01	α'
64	0.18	32.89	0.10	1.47	γ
65	0.18	32.17	0.10	3.02	γ
66	0.18	28.54	0.10	0.97	γ
67	0.18	22.66	8.78	2.56	γ
68	0.17	26.40	0.10	3.75	γ
69	0.20	21.89	0.10	4.46	γ
70	0.19	29.87	0.10	4.87	γ
71	0.18	28.22	5.97	5.01	γ
72	0.18	27.26	9.56	4.96	γ
73	0.19	32.37	0.10	0.10	γ
74	0.18	22.32	0.10	5.46	γ
75	0.20	31.10	0.10	7.61	γ
76	0.21	22.42	0.10	7.22	γ
77	0.18	32.41	0.10	6.92	γ
78	0.22	15.17	0.10	0.12	$\gamma+\epsilon$
79	0.18	13.33	0.10	1.01	$\gamma+\epsilon$
80	0.18	20.78	0.10	0.13	$\gamma+\epsilon$

Table V. Composition/Microstructure Results for Fe-Al-Mn-Ni Weld Metal (Continued)

Sample No.	C wt%	Mn wt%	Ni wt%	Al wt%	Microstructure
81	0.19	24.66	0.10	0.26	$\gamma + \epsilon$
82	0.21	15.09	0.10	5.07	$\gamma + \alpha$
83	0.20	17.92	0.10	4.99	$\gamma + \alpha$
84	0.18	17.86	0.10	7.00	$\gamma + \alpha$
85	0.19	18.77	0.10	5.26	$\gamma + \alpha$
86	0.22	24.74	0.10	6.62	$\gamma + \alpha$
87	0.18	22.46	0.10	7.84	$\gamma + \alpha$
88	0.18	7.03	0.10	6.03	α
89	0.20	11.99	0.10	7.87	α
90	0.21	32.41	0.10	8.43	$\gamma + \alpha$
91	0.19	15.66	0.10	3.03	$\gamma + \alpha'$
92	0.19	15.12	0.10	3.82	$\gamma + \alpha'$

II.2 Technique of Microstructural Characterization

Weld metal microstructures were analyzed for austenite, ferrite, α' martensite and ϵ martensite by x-ray diffraction and optical microscopy. The x-ray diffraction method is well suited to differentiating between the FCC crystal structure of austenite, the HCP crystal structure of ϵ martensite and the BCC/BCT crystal structure of ferrite and α' martensite. Detecting the presence of ferrite in association with α' martensite is difficult as the martensite doublets are not usually resolvable. Such determinations were made through the use of optical microscopy in this investigation.

X-ray diffraction structural analysis employed a Phillips wide range vertical goniometer with a copper $K\alpha$ source. A bent graphite crystal monochromator was used to eliminate the high fluorescent background. Where high temperature diffraction data were required a Phillips horizontal goniometer fitted with an environmental chamber was employed. Specimens were resistance heated in a helium atmosphere to avoid contamination.

Intensity vs two theta plots were collected. These results were interpreted through the use of Braggs Law and the indexing procedure described by Klug and Alexander (24). The volume percentages of each phase were estimated by comparing the integrated diffraction intensities of the (200)

and (211) alpha peaks and the (200) and (220) gamma peaks. The presence of the (1012) epsilon peak was used to detect epsilon martensite formation. Cullity (25) discusses the method of quantitative analysis which may be outlined as follows. Quantitative analysis by diffraction is based on the fact that the intensity of the diffraction pattern for a particular phase in a mixture of phases is concentration dependent. For the diffractometer this dependence is:

$$I = \frac{I_0 A \lambda^3}{32 \pi r} \left(\left(\frac{\mu_0}{4\pi} \right) \frac{e^4}{m^2} \left(\frac{1}{V^2} \right) \right) \left((F)^2_p \left(1 + \frac{\cos^2 2\theta}{\sin^2 \theta \cos \theta} \right) \right) \frac{e^{-2m}}{2\mu} \quad (1)$$

where

- I = integrated intensity (joules $\text{sec}^{-1} \text{m}^{-1}$)
- I_0 = intensity of the incident beam (joules $\text{sec}^{-1} \text{m}^{-2}$)
- A = cross-section area of incident beam (m^2)
- λ = wavelength of incident beam (m)
- r = radius of diffraction circle (m)
- μ_0 = $4\pi \times 10^{-7}$ (mkg C^{-2})
- e = charge on electron (C)
- m = mass of e^- (kg)
- V = volume of unit cell (m^3)
- F = structure factor

P = multiplicity factor
 θ = Bragg Angle
 e^{-2m} = temperature factor
 μ = linear absorption coefficient (m^{-1})

Using the direct comparison method equation I can be simplified:

$$K = \left(\frac{I_0 A \lambda^3}{32 \pi r} \right) \left(\left(\frac{\mu_0}{4 \pi} \right) \frac{e^4}{m} \right) \quad (2)$$

$$R = \frac{1}{V^2} \left((F)^2 P \left(\frac{1 + \cos^2 2\theta}{\sin^2 \theta \cos \theta} \right) \right) \left(\frac{e^{-2m}}{2\mu} \right) \quad (3)$$

Substituting equation 2 and equation 3 into equation 1 gives

$$I = KR \quad (4)$$

Where I is the diffracted intensity, K is a constant, R depends on θ , hkl and the kind of substance.

Rewriting equation 4 for a particular diffraction line

$$I_{\gamma} = K R_{\gamma} V_{\gamma} \quad (5)$$

$$I_{\alpha} = KR_{\alpha}V_{\alpha} \quad (6)$$

Where V is the volume percent of the alpha and gamma phases.

Division of equation 5 by equation 6 yields

$$\frac{I_{\gamma}}{I_{\alpha}} = \frac{R_{\gamma}V_{\gamma}}{R_{\alpha}V_{\alpha}}$$

Thus V_{γ}/V_{α} is obtained from the measurement of I_{γ}/I_{α} and calculation of R_{γ} and R_{α} . The calculation of R requires a knowledge of the crystal structure and lattice parameters of both phases. Troieno and McGuire's (26) data of a_0 (gamma) = 3.584A and a_0 (alpha) = 2.862A were used to calculate the unit cell volumes. Although it is recognized that lattice parameters are a function of alloy content it is felt that these values give reasonable values for the volume percentages of the austenite and ferrite phases. The temperature factors were taken from Figure 12.

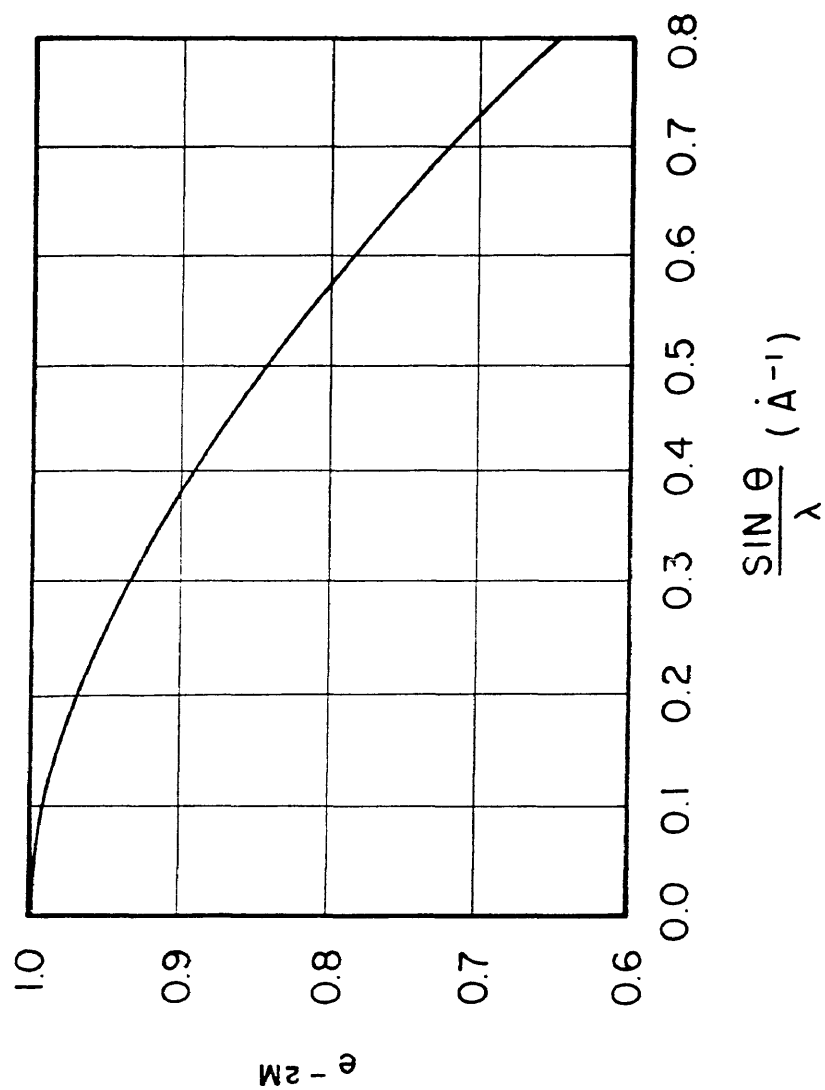


Figure 12. Temperature factor $\exp(-2M)$ of iron at 20°C as a function of $(\sin \theta)/\lambda$ (24).

III. RESULTS AND DISCUSSION

An extensive metallographic investigation was performed in an attempt to characterize the nature of the phase transformations that occur in Fe-Al-Mn-Ni weldments. The morphology and crystal structure of the various phases in over ninety fusion zone microstructures were identified by hot-stage x-ray diffractometry, dilatometry and optical microscopy. These results are presented in Table V.

Characteristic microstructures for a few of the compositions investigated are presented in Figures 13 and 14. Figure 13 shows the effect of increasing aluminum content on microstructures for weldments having constant nickel and manganese concentrations. The martensitic transformation dominated at 1.5 weight percent aluminum (Figure 13a). Patches of martensite outlined by discontinuous ferrite are observed in the five weight percent aluminum alloy (Figure 13b). Raising the aluminum concentration to seven weight percent (Figure 13c) results in a dominantly ferritic microstructure. A grain boundary phase with a Widmanstätten morphology is also seen in this microstructure. Microdiffractometry has shown this phase to have a lattice parameter close to that of the ferrite grain. Figure 14 illustrates the microstructural variation encountered when increasing

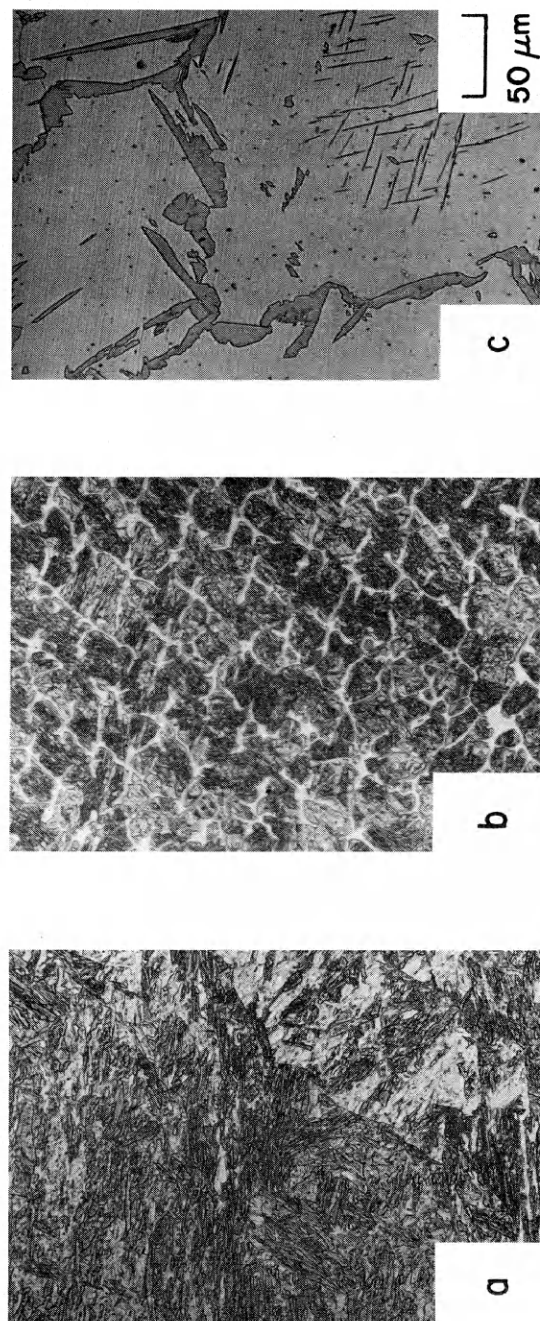


Figure 13. Effect of increasing aluminum content for weld metal having a nickel equivalent of 20. a) 1.5 wt% Al b) 5.0 wt% Al c) 7.0 wt% Al.

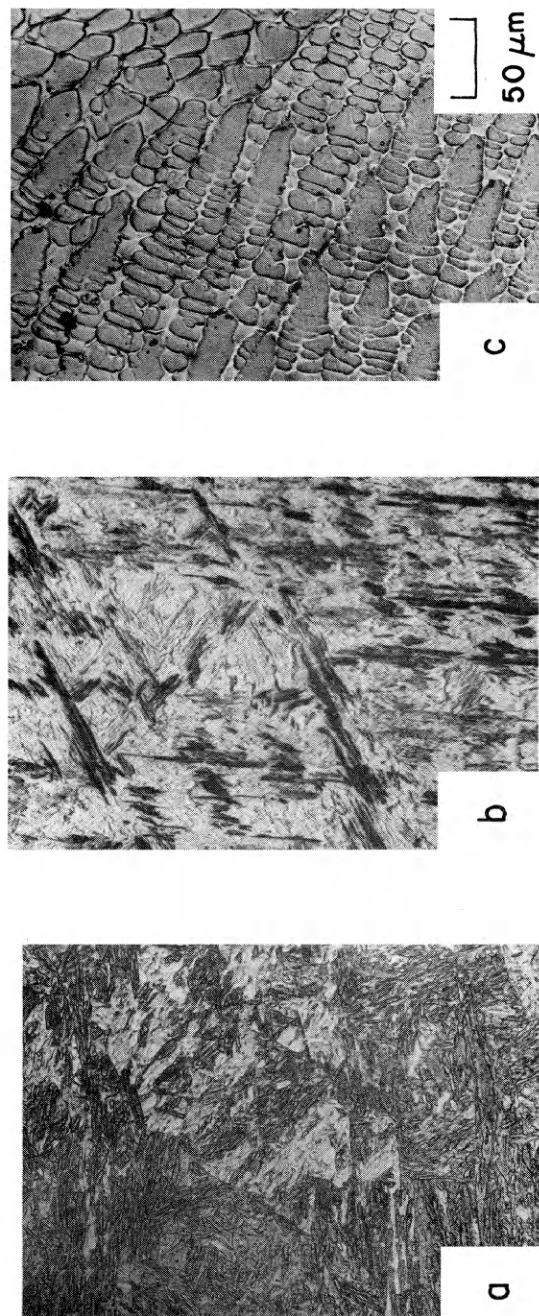


Figure 14. Effect of increasing nickel equivalent for weld metal containing 1.5 weight percent aluminum. a) 20 b) 30 c) 70.

the amount of austenitic stabilizer to a Fe-1.5 wt% Al alloy. A Ni_{eq} of 20 resulted in the fully martensitic microstructure shown in Figure 14a. Two phase austenite plus martensite microstructure was found when the Ni_{eq} was raised to 30. Fully austenite microstructures were encountered at a Ni_{eq} of 70. Duplex microstructures of austenite and ferrite were observed in weldments containing six weight percent aluminum with a Ni_{eq} of 32 as shown in Figure 15.

Alloying elements in iron-based systems influence the amounts of ferrite and austenite which form as well as the martensite start temperature. These effects may be summarized for non-equilibrium conditions inherent in welding processes through the use of a Schaeffler diagram (27). The Schaeffler diagram (Figure 16) is used to predict weld metal microstructures which influence mechanical and physical properties. The effect of the austenite stabilizing elements, such as nickel, manganese and carbon, are summed together in terms of a Ni_{eq} equation and plotted on the vertical axis. Similarly the effects of ferrite stabilizing elements, such as chromium, molybdenum, silicon and niobium, are summed together in a Cr_{eq} equation and plotted along the horizontal axis. Regions of stable phases are identified and plotted as a function of composition. The phase fields being austenite, austenite plus martensite and martensite indi-

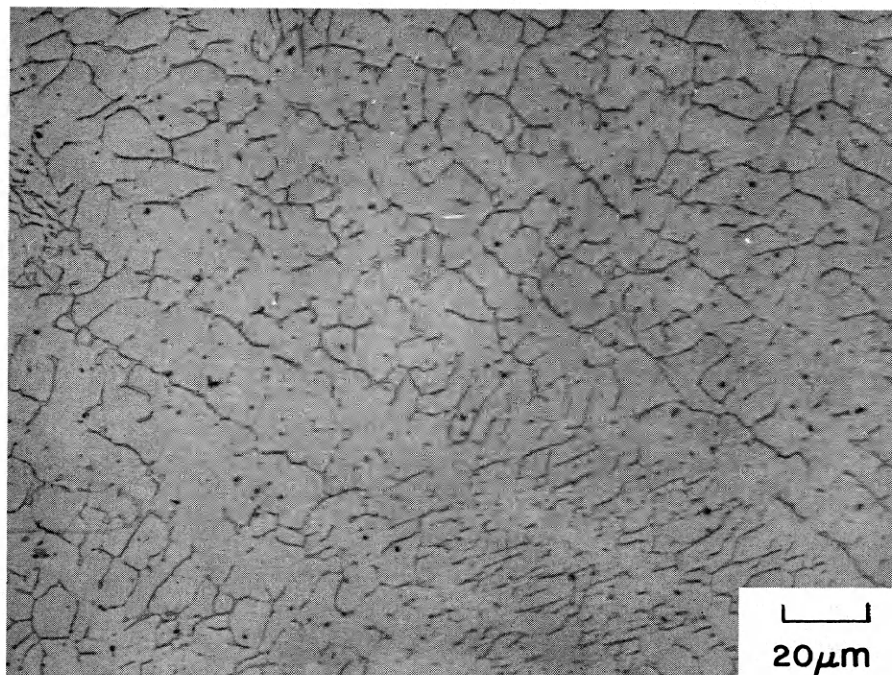


Figure 15. Microstructure of weld metal containing 6 wt% aluminum and a nickel equivalent of 32. Austenite and "delta type" ferrite are observed.

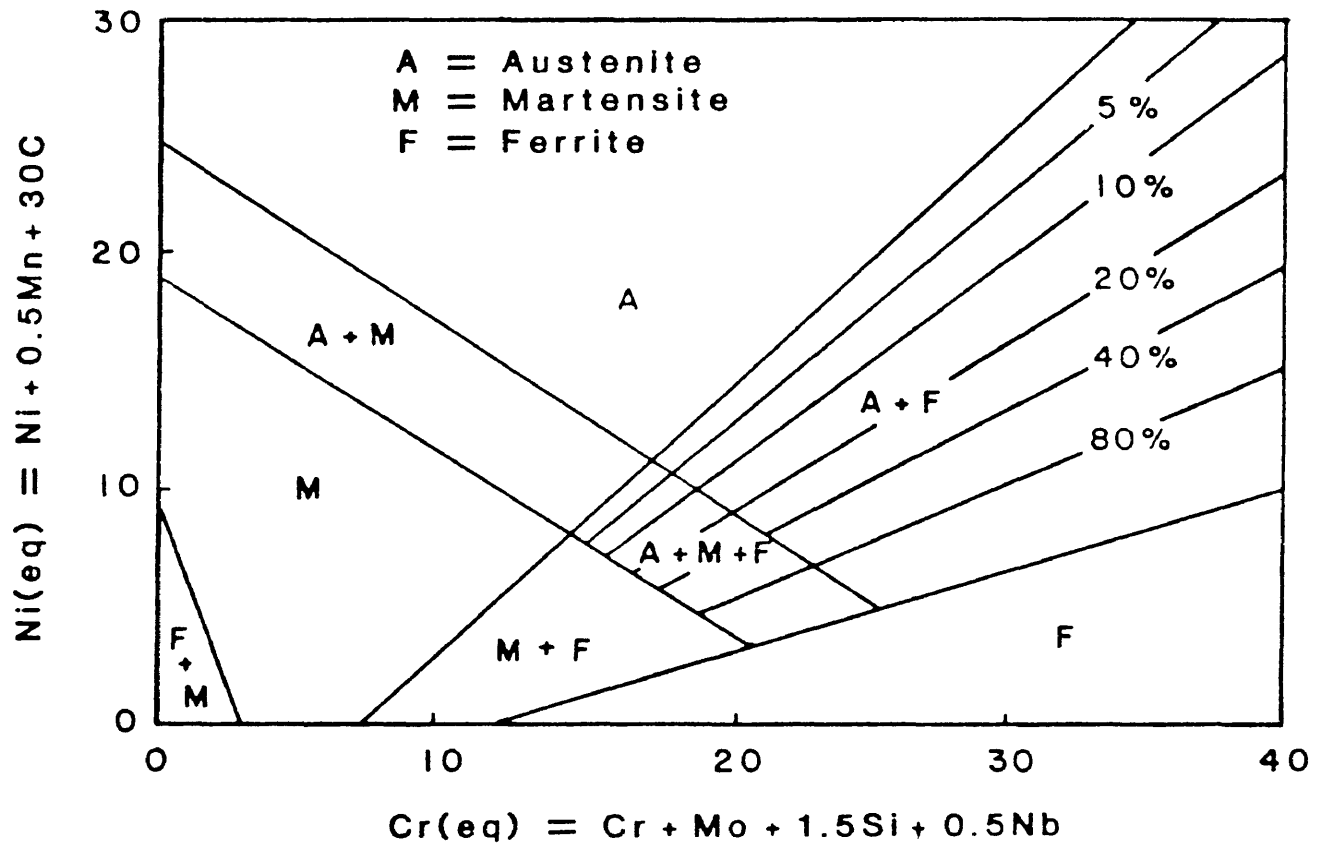


Figure 16. The Schaeffler diagram for weld metal microstructure.

cated on the left hand side of the diagram. Austenite, austenite plus ferrite and ferrite phase fields are plotted on the right hand side of the diagram.

III.1 Schaeffler Type Diagram for Fe-Al-Mn-Ni Weld Metal

Figure 17 is a proposed Schaeffler type diagram developed from the microstructural characterization and bulk chemical analysis for these Fe-Mn-Ni-Al weldments. The diagram can be divided into regions of austenite-martensite and austenite-ferrite transformations on the left and right side of the diagram respectively. Stable austenite was found to exist at room temperature for alloys having a Ni_{eq} in excess of 60. The minimum composition for an austenite alloy was found at Fe-5wt%Al-48 Ni_{eq} .

With reductions in the Ni_{eq} , the martensitic transformations for weldments containing less than five weight percent aluminum resulted in two phase, austenite plus martensite microstructures. Two types of martensite have been identified within this field. These were the conventional BCT (α') type observed in many ferrous materials and the HCP form referred to as epsilon (ϵ) martensite. Epsilon martensite is non-magnetic and is difficult to define clearly by optical microscopy. The identification of epsilon martensite requires the use of dilatometric and diffraction techniques.

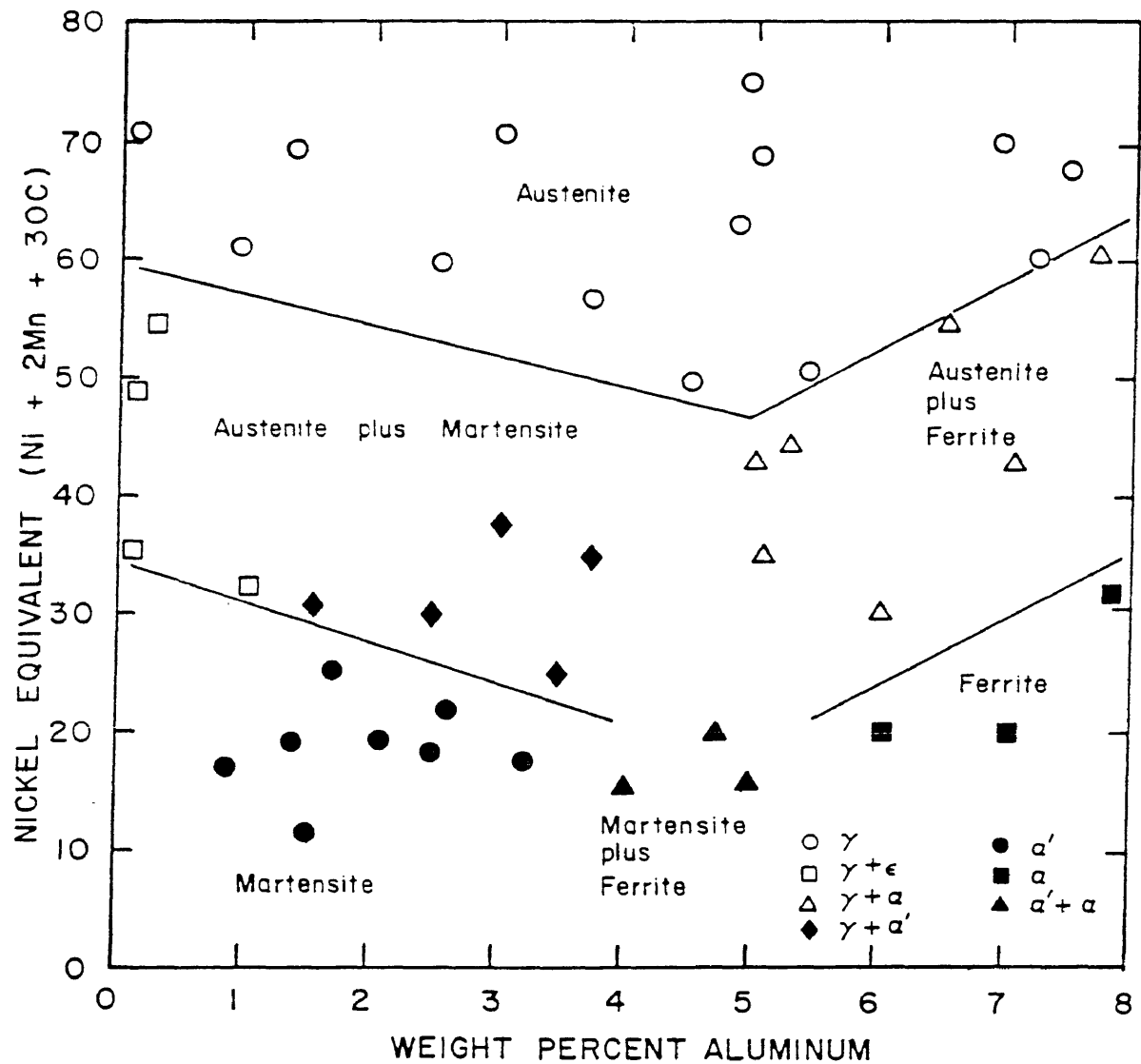


Figure 17. "Schaeffler-type" diagram for Fe-Al-Mn-Ni weldments.

Troiano and McGuire (26) have determined the lattice parameters of austenite and epsilon phases as a_0 is 3.584 Å and c/a is 1.605 respectively. Their calculation of the density for each phase from these measurements show that epsilon martensite is more closely packed than austenite. Gordon-Parr (28) and Schmidt (29) show similar results in the Fe-Mn-Cr alloy system. Thus upon cooling the γ - ϵ transformation results in a lattice contraction. The formation of a BCC type crystal structure from austenite whether it be ferrite or α' martensite involves a lattice expansion.

A Gleeble thermo-mechanical testing system has been used to make dilatometric measurements of a 1.5 wt% Al-30 Ni_{eq} alloy. These results are reported in Figure 18. This type of behavior can be accounted for by considering the alloy to be austenitic at 800°C. Upon cooling to 200°C the martensitic reaction γ - α' results in the observed expansion. Figure 14 gives microstructural evidence of the martensitic reaction. This reaction was apparently interrupted by the formation of epsilon martensite as indicated by the sharp transition in the dilatometry curve at the epsilon start (ϵ_s) temperature of 150°C.

X-ray diffractometry was employed to support the dilatometric results. Room temperature diffraction patterns revealed the presence of the $(1011)\epsilon$, $(1012)\epsilon$, $(200)\alpha'$ and

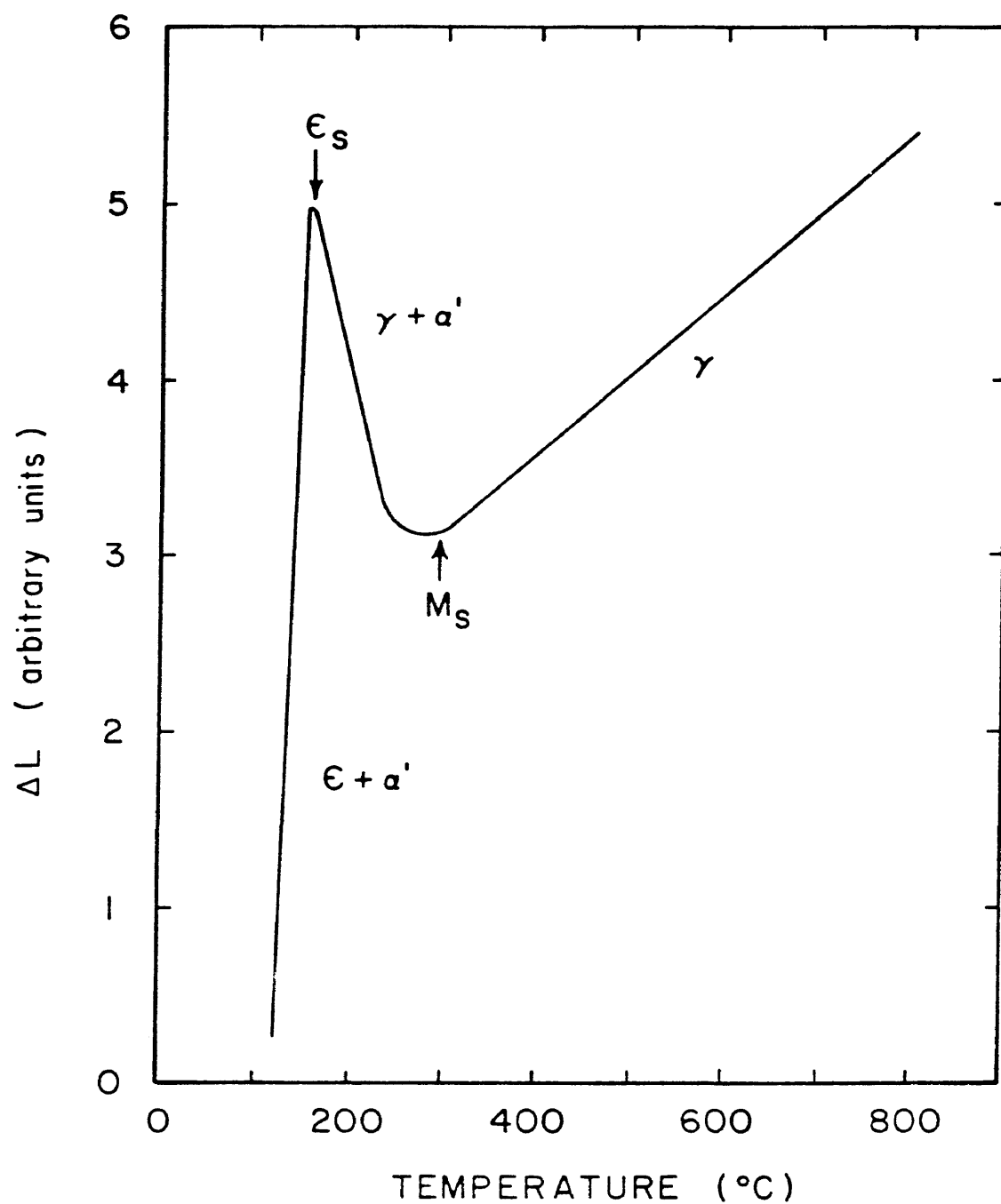


Figure 18. Dilatometric curve for a 1.5 wt% Al - 32 Ni alloy cooled from 800 $^{\circ}\text{C}$. The epsilon start (ϵ_s) and α' -martensite start (M_s) temperatures are indicated.

(211) α peaks. Characteristic peaks for austenite were also present but these were much less intense than those characteristic of the α' and ϵ phases. Diffraction patterns collected at 800°C showed a substantial increase in the intensity of the (220) γ peak. These results and the dilatometry support the idea that this alloy solidified as primary austenite and remained austenitic to the M_s temperature. The fact that the ϵ phase did not form until after the α' transformation suggests the following reactions:

(first) austenite transforming to α' martensite

(second) austenite transforming to ϵ martensite

This series of reactions implies that the α' and ϵ transformations occur as independent processes. There is also the possibility that these phases are the result of parallel reactions. If true, the magnitude of the α' transformation dominated over the ϵ transformation until the weldment cooled to 150°C where ϵ became more dominate.

In Fe-Cr-Ni alloys ϵ martensite has been found in conjunction with α' martensite. As such researchers have directed their attention towards determining whether or not epsilon martensite is an intermediate phase to the formation of α' martensite or a separate constituent which could form

as a result of the strain generated by the γ - α' transformation. Venables (30) and Olson and Cohen (31) have shown formation of α' needles at intersections of ϵ martensite plates. Cina (32) Reed (33) and Breedis and Robertson (34) also reported the hcp structure to be an intermediate phase in the formation of α' martensite. Dash and Otte (35) reported instances of independent formation of the two phases and summarized the various possibilities in Figure 19. Dash and Otte reported that based on the morphology of the ϵ phase its formation appears to be incidental to the formation of α' . Microstructural evidence of the ϵ - α' type transformation has not been found in this investigation.

III.2 Development of a Martensite Start Equation

The martensite transformation is a function of composition such that all elements tend to decrease the M_s temperature. The most complete analysis of this functionality was performed by Andrews (36). The Andrews equation is given as follows:

$$M_s(^{\circ}C) = 539 - 423C - 30.4Mn - 12.1Cr - 17.5Ni - 7.5Mo \quad (7)$$

It has been assumed that no synergistic effects occur between elements. Using a similar form of the Andrews Equation the

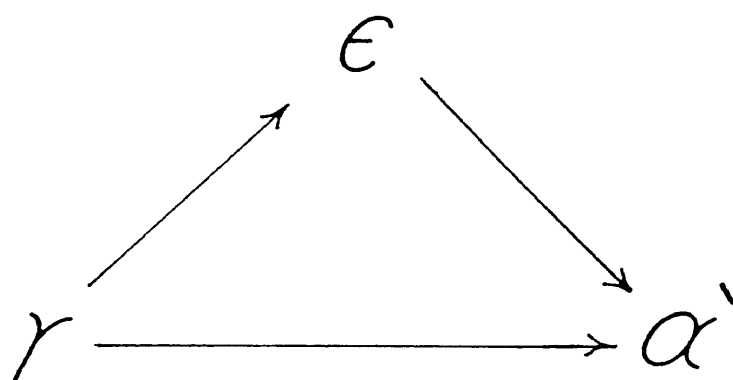


Figure 19. Hypothetical paths for the formation of α' martensite from austenite (33).

α' transformation has been characterized for Fe-Al-Mn-Ni weld metal. The composition ranges for which this equation has been determined are for a Ni_{eq} between ten to thirty and aluminum content between zero to four weight percent. All of these alloys had fully α' martensitic microstructures, some contained a small percentage of austenite. Epsilon martensite was not detected. Table VI lists the experimental results used to derive the M_s equation. Multivariable regression on these data gives:

$$M_s(^{\circ}C) = 583 - 417C - 14.6Ni - 29.2Mn - 53Al \quad (8)$$

Where a coefficient of 53 has been assigned for the ability of aluminum to suppress the M_s temperature. The other coefficients for carbon, nickel and manganese are slightly different from those determined by Andrews (36).

Wetting the martensite temperature equal to $20^{\circ}C$ and grouping carbon, nickel and manganese terms together in a Ni_{eq} expression results in the following:

$$40 = Ni_{eq} + 3.6Al \quad (9)$$

A plot of Equation 9 on the "Schaeffler type" diagram is shown in Figure 20. Weld metal with a composition below this

Table VI. Martensite Start Data for Various Weld Metal Compositions

Specimen Number	Ms($^{\circ}$ C)	Al(wt%)	Mn(wt%)	Ni(wt%)	C(wt%)
4	260	1.35	6.30	--	0.18
5	155	3.01	6.16	--	0.18
7	115	1.99	9.50	--	0.14
12	240	2.86	2.79	1.72	0.19
13	210	3.26	2.93	3.14	0.19
14	175	3.14	2.99	5.68	0.19
27	130	1.67	8.80	2.61	0.18
11	190	2.08	3.69	6.72	0.17
21	190	2.08	3.69	6.72	0.17
23	180	2.71	4.66	3.85	0.19

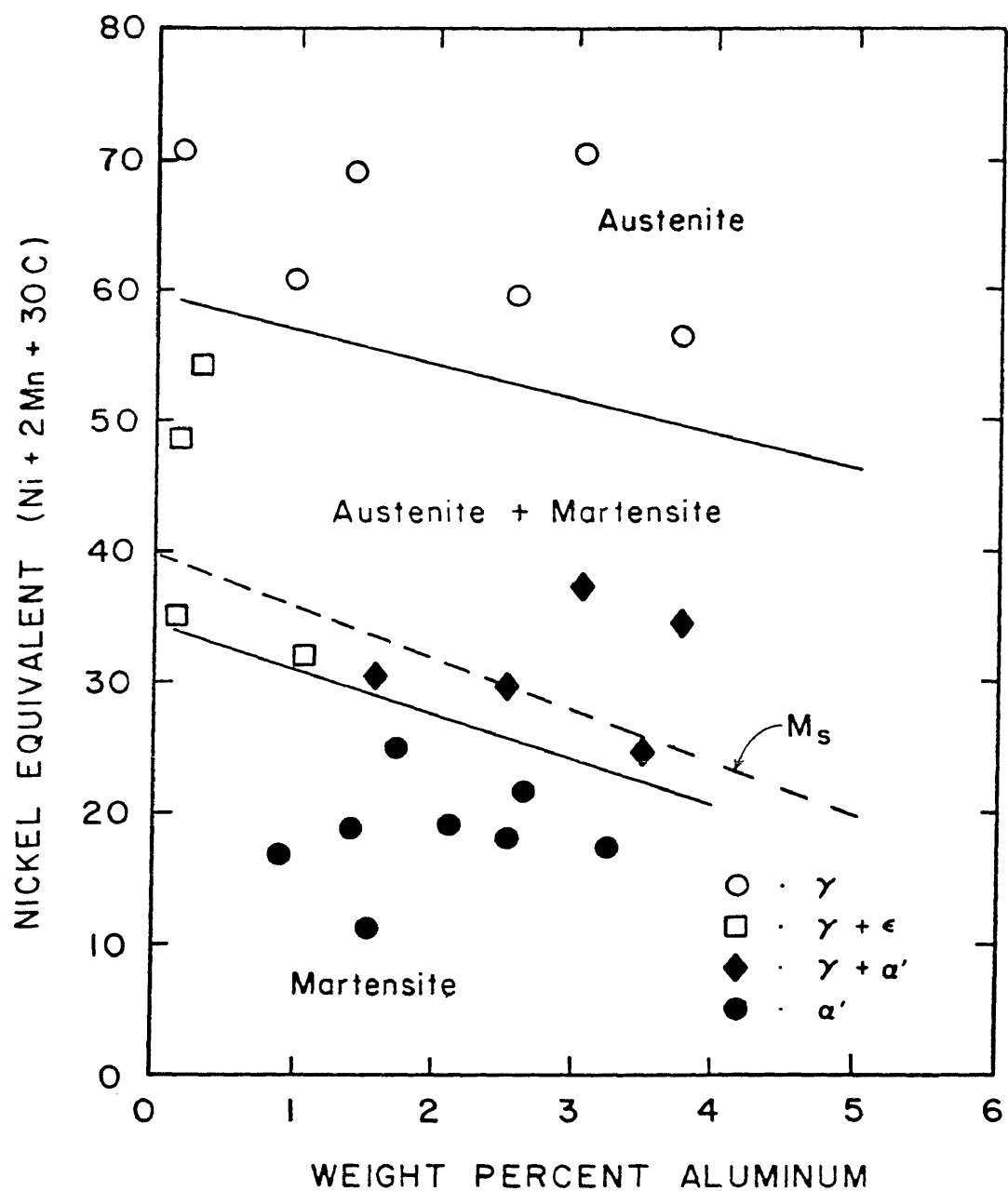


Figure 20. Martensite start line superimposed on the Schaeffler diagram for Fe-Mn-Ni-Al weld metal.

line will transform to α' martensite at room temperature. It is observed that weld metal with a composition above this line however, also has some percentage of martensite. This observation can be accounted for by considering the ϵ martensite reaction to have a higher start temperature than the α' martensite reaction. Thus additional alloying addition is required to produce a stable austenitic microstructure.

From Equation 9 it is apparent that the value of 3.6Al can represent the aluminum contribution to the chromium equivalent equation. Rewriting Schaeffler's original chromium equivalent, Cr_{eq} , expression to include this term results in:

$$Cr_{eq} = Cr + Mo + 1.55 + 0.5Nb + 3.6Al \quad (10)$$

Whereas Schaeffler's Cr_{eq} equation was applied over a wide range of compositions. This equation, more specifically the coefficient for aluminum, was developed for weld metal containing less than five weight percent aluminum. Table VII gives the results of other investigators (37-40) who have reported coefficients for aluminum of 2.48 to 5.00 in stainless steels containing up to 1.5 weight percent aluminum. The value of 3.60 determined in this investigation lies between Guiraldeng's value of 3.00 and Potak's value of 4.00.

Table VII. Chromium Equivalent Coefficients for Aluminum

Investigator	Cr _{eq}	References
Hull	2.48	37
Guiraldeng	3.00	38
Potak	4.00	39
Schneider	5.00	40

III.3 Ferritic Transformation

Figure 17 identifies three regions of phase stability for alloys containing in excess of five weight percent aluminum. Those weldments with a low Ni_{eq} were ferritic. Increasing the concentration of austenite stabilizers resulted in duplex austenite plus ferrite microstructures. Fully austenitic microstructures were encountered with further increases in Ni_{eq} .

The proportion of austenite and ferrite formers govern the solidification behavior and mechanism of ferrite decomposition in these alloys. A qualitative understanding of the possible phase transformations can be made by considering an isopleth developed for Fe-Ni-Al alloys. X-ray diffraction analysis results have not indicated the presence of beta manganese or ordered phases. Thus the 30 weight percent nickel isopleth (Figure 8h) determined by Bradley (13) has been simplified to consist of austenite, ferrite and austenite plus ferrite phase fields. Manganese is expected to act as an austenite stabilizer and therefore can be added to the nickel concentration in terms of a nickel equivalent. The basic features of the isopleth are not expected to change dramatically with manganese additions. Figure 21 illustrates the simplified isopleth used to predict phase transformations.

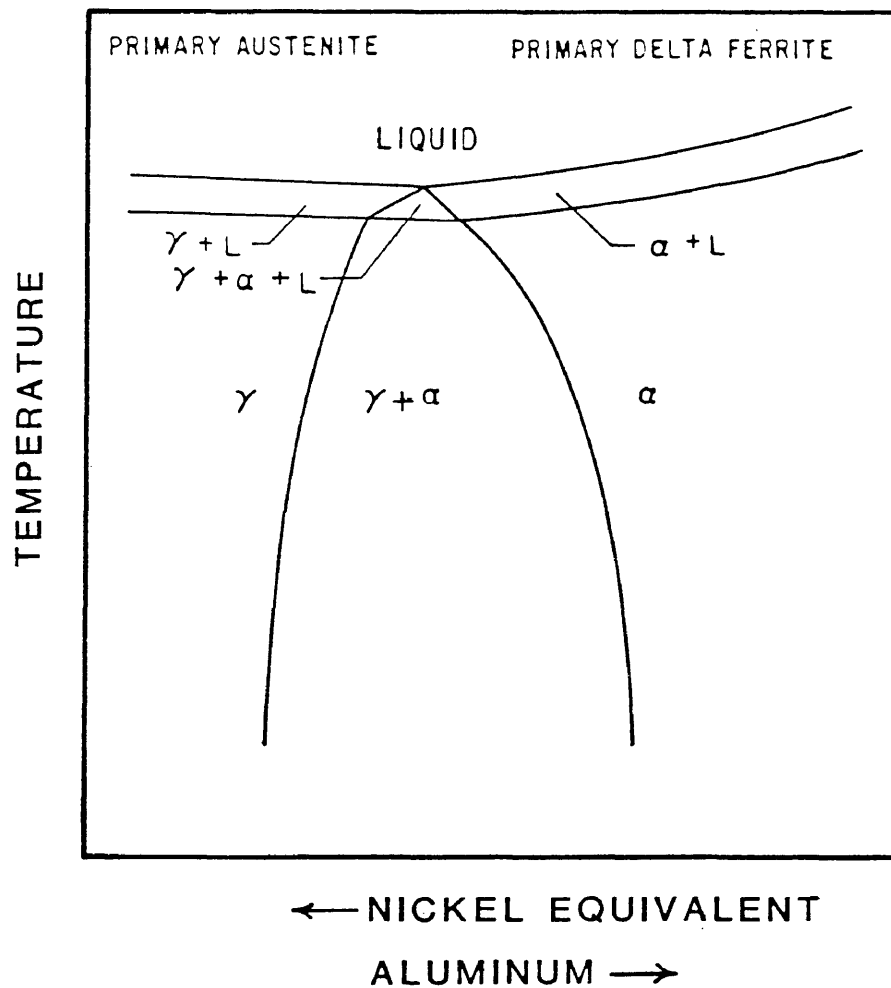


Figure 21. Isopleth used to predict phase transformations in Fe-Al-Mn-Ni weld metal.

Weld metal compositions falling to the left of the eutectic triangle (hypo-pseudo-eutectic) solidify as primary austenite. The austenite will transform martensitically if there is insufficient alloying to suppress the martensite start temperature below room temperature. Ferrite, if any, will form between dendrites of austenite due to the segregation of aluminum to the liquid during freezing. The final liquid will solidify as a $\gamma + \alpha$ divorced eutectic. There is also the possibility of a solid state $\gamma - \alpha$ reaction. Evidence of these two phenomena were not found in the microstructures examined however.

Weld metal, whose composition lies to the right of the eutectic triangle (hyper-pseudo-eutectic), will begin to solidify as primary ferrite. Compositions of alloys within the $\gamma + \alpha$ phase field may transform to austenite by a $\alpha - \gamma$ solid state transformation. The microstructure in Figure 15 is representative of Fe-6wtTA1-32Ni_{eq} alloy which has solidified primarily as ferrite and then transformed to austenite upon cooling. The results of high temperature x-ray diffraction performed on this specimen confirm the solid state transformation. These are given in Table VIII. At 1200°C the sample is ferrite. Cooling to 700°C reduces the volume percent ferrite to 24 with a corresponding increase in the volume percent of austenite to 76. X-ray diffraction

Table VIII: High Temperature X-Ray Diffraction Results

Temperature ($^{\circ}\text{C}$)	Vol. % α	Vol. % γ
1200	100	--
700	24	76
20	11	89

performed at room temperature indicates 11 volume percent ferrite and 89 volume percent austenite.

Compositions of the ferrite and austenite phases were obtained through the use of a scanning electron microscope equipped with an energy dispersive detector. A fundamental parameter program was used to determine the weight percentage of aluminum, manganese, nickel, and iron for each phase. The precision for an individual measurement ranged from 0.5 percent to 3 percent relative. The accuracy predicted from the etched surface will approach five percent relative. The results reported in Table IX indicate that the ferrite is rich in aluminum and leaner in manganese. The nickel concentration was approximately the same for both phases.

The microstructure in Figure 15 and the proposed transformation sequence is analogous to that found in stainless steel (41-43) having $1.48 \leq \text{Cr}_{\text{eq}}/\text{Ni}_{\text{eq}} \leq 1.95$. This type of microstructure is of interest because its morphology is similar to that formed in stainless steel welding when using type 308 stainless steel filler wire. Based upon the properties associated with this type of microstructure in stainless steels it is anticipated that weld metal with a austenite plus aluminum rich ferrite microstructure will have a low crack susceptibility and be resistant to hot tearing.

Table IX. Analytical Compositions (weight percent) for Weld Metal Containing 6 wt% Al with a Nickel Equivalent of 32.

	Al	Mn	Ni	Fe
Ferrite	7.25	9.05	4.24	85.4
Austenite	5.54	10.89	4.93	81.7

IV. CONCLUSIONS

1. Fe-Al-Ni-Mn alloys appear to be viable alternatives to stainless steel. Desirable weld metal microstructures have been produced in the fusion zone.
2. Regions of phase stability have been identified and plotted on a Schaeffler type diagram. Although refinement of this diagram is necessary it is expected to be a viable tool in welding Fe-Al-Mn-Ni materials.
3. Weld metal containing less than five weight percent aluminum transform martensitically if insufficient alloy has been added to suppress the martensite start temperature below room temperature. Two types of martensite have been identified α' martensite with a BCT crystal structure and ϵ martensite with a HCP crystal structure. A M_s equation for α' martensite has been developed and from this a chromium equivalent equation involving aluminum. The coefficient for aluminum was found to be 3.6 which falls between the values reported in the literature for Fe-Cr-Al-Ni alloys.
4. Alloys containing an excess of five weight percent aluminum involve ferrite transformations. It has been demonstrated that weld metal can solidify as primary ferrite and then transform to austenite by a solid state reaction.

V. REFERENCES

1. "Contingency Plans for Chromium Utilization", Publication #NMAB-335, National Academy of Sciences, Washington, D.C. 20418, 1978.
2. P. Tomaszewicz and G.R. Wallwork, "The Oxidation of Fe-Al Alloys Containing Cr, Ni or Mn", Corrosion-NACE, Vol. 40, No. 4, April 1984, p. 152-157.
3. M. Sakiyuma, P. Tomaszewicz and G.R. Wallwork, Oxide. Met., Vol. 13, No. 4, 1979, p. 311.
4. P.R.S. Jackson and G.R. Wallwork, Proceedings of the 35th Annual Conference of Aus. Inst. of Metals, Sydney, 1982, p. 78-81.
5. P. Tomas, "Elements Essential to High Temperature Sulfidation Resistant Iron-Based Alloys", Univ. of New South Wales, Kensington, NSW Australia, Proc. 35th Annual Conf. of the Australian Inst. of Metals, Sydney, May 1982, p. 90.
6. R.A. Perkins, Quarterly Report E-2299-6, Lockheed, Palo Alto Research Laboratory, 1976.
7. Rosie Wang and Franklin H. Beck, "New Stainless Steel Without Nickel or Chromium for Marine Applications", Metals Progress, March 1983, p. 72-76.
8. W. Koster and W. Tonn, "The Iron Corner of the Iron-Manganese-Aluminum System", Archiv. fur Eishenhuttenwesen, Vol. 7, 1933-1934, p. 365.
9. D.J. Schmatz, "Formation of Beta Manganese-Type Structure in Iron-Aluminum-Manganese Alloys", Trans. AIME, Vol. 215, Feb. 1959, pp. 112-114.
10. W. Koster, "The Iron Corner of the Iron-Nickel-Aluminum System", Archiv, fur Eisenhuttenwesen, Vol. 7, 1933, p. 257.
11. A.J. Bradley, "Microscopical Studies on the Fe-Ni-Al System - Part I", JISI, Sept. 1949, pp. 19-30.
12. A.J. Bradley and A. Taylor, Physics in Industry, Magnetism, 1938, p. 89.

13. A.J. Bradley, "Microscopical Studies on the Fe-Ni-Al System - Part II", JISI, Sept. 1949, p. 27.
14. A.J. Bradley, "Microscopic Studies on the Fe-Ni-Al System - Part III", JISI, May 1952, p. 42.
15. D.J. Schmatz, "Structure and Properties of Austenite Alloys Containing Aluminum and Silicon," Trans ASM, Vol. 52, 1960, pp. 898-913.
16. J. Charles and A. Berghezan, "Nickel-Free Austenite Steel for Cryogenic Applications: The Fe-24%Mn-5%Al-0.2%C alloys", Cryogenics, Vol. 21, May 1981, pp. 278-280.
17. H. Schemann, "Zusammenhang zwischen Gefugeaufloau and un anderen Eigenschaften Kohlenstoffarmer Manganstahle", Arch. Eisenhuettenw, Vol. 38, No. 8, 1967, pp. 647-656.
18. H. Schumann, "Die martensitischen Umwandlunger in Kohlenstoffarmen Manganstahlen", Arch. Eisenhuettenw, Vol. 38, No. 9, 1967, pp. 743-749.
19. A. Holden, J.D. Bolton, and E.R. Petty, "Structure and Properties of Iron-Manganese Alloys", JISI Lond., Vol. 209, 1971, pp. 721-727.
20. S. Case and K. VanHorn, Aluminum in Iron and Steel, Wiley, 1952, p. 265.
21. F. Weaver, Archiv. Eisenhuttenw, Vol. 2, 1928-29, p. 739.
22. K.W. Andrews, "The Calculation of Transformation Temperatures and Austenite-Ferrite Equilibria in Steels", JISI (London), Vol. 184, 1956, p. 414.
23. C. Zener, "Equilibrium Relations in Medium-Alloy Steels", Trans. AIME, Vol. 167, 1946, pp. 513-534.
24. H.P. Klug, L.E. Alexander, X-Ray Diffraction Procedures, John Wiley and Sons, New York, 1974, pp. 419-446.
25. B.D. Cullity, Elements of X-Ray Diffraction, Addison-Wesley Publishing, Mass., 1978, pp. 389-415.

26. A.R. Troiano and F.T. McGuire, "A Study of the Iron-Rich Manganese Alloys", Trans. ASM, Vol. 31, 1943, p. 355.
27. A.L. Schaeffler, "Constitutional Diagram for Stainless Steel Weld Metal", Met. Prog., Vol. 56, 1949, pp. 680.
28. J. Gordon-Parr, "X-Ray Investigation of the Epsilon Phase in an Fe-Mn Alloy", JISI, Vol. 171, 1952, p. 137.
29. W. Schmidt, "Rontgenographische Untersuchungen uber das System Eisen-Mangan". Archiv. fur das Eisenhuettenwesen, Vol. 3, 1929, p. 293.
30. J.A. Venables, "The Martensitic Transformation in Stainless Steel", Phil. Mag., Vol. 7, 1962, p. 35.
31. G.B. Olson and M. Cohen, "Kinetics of Strain-Induced Martensitic Nucleation", Met. Trans., Vol. 6A, 1975, p. 791.
32. B. Cina, "A Transitional hcp Phase in the γ - α Transformation in Certain Fe-Base Alloys", Acta Metall., Vol. 6, 1958, p. 748.
33. R.P. Reed, "The Spontaneous Martensitic Transformations in 18% Cr, 8% Ni Steels", Acta Metall., Vol. 10, 1962, p. 865.
34. J.F. Breedis and W.D. Robertson, "The Martensitic Transformation in Single Crystals of Iron-Chromium-Nickel Alloys", Acta Met., Vol. 10, 1962, pp. 1077.
35. J. Dash and H.M. Otte, "The Martensite Transformation in Stainless Steel", Acta Met., Vol. 11, 1963, p. 1169-1178.
36. K.W. Andrews, "Empirical Formulae for the Calculation of Some Transformation Temperatures", JISI, Vol. 203, 1965, pp. 721-727.
37. F.C. Hull, "Delta Ferrite and Martensite Formation in Stainless Steels", Welding Journal, Vol. 52, No. 5, 1973, pp. 1935-2035.

38. P. Guiraldeng, "Ferrite and Austenite Forming Tendencies on the Principle Alloying Elements in 18Cr-10Ni Stainless Steel", *Revue de Metallurgie, Memoires Scientifiques*, (Part 1), Vol. 64, No. 11, 1967, pp. 907-939.
39. M. Potak and E.A. Sagalevich, "Structural Diagram for Stainless Steels as Applied to Cast Metal and Metal Deposited During Welding", *Avt Svarka*, Vol. 5, 1972, pp. 10-13.
40. H. Schneider, "Investment Casting of High-Hot Strength 12% Chrome Steel", *Foundry Trade J.*, Vol. 108, 1960, pp. 562-563.
41. T. Takalo, N. Suutala and T. Moisio, "Austenitic Solidification Mode in Austenitic Stainless Steel Welds", *Met. Trans.*, 10A, August 1979, pp. 1173-1181.
42. N. Suutala, T. Takalo and T. Moisio, "Single-Phase Ferritic Solidification Mode in Austenitic-Ferritic Stainless Steel Welds", *Metall. Trans.*, 10A, August 1979, pp. 1183-1190.
43. N. Suutala, T. Takalo and T. Moisio, "Ferritic-Austenitic Solidification Mode in Austenitic Stainless Steel Welds", *Met. Trans.*, Vol. 11A, May 1980, pp. 717-725.